ELSEVIER

Contents lists available at ScienceDirect

Journal of Colloid and Interface Science

journal homepage: www.elsevier.com/locate/jcis

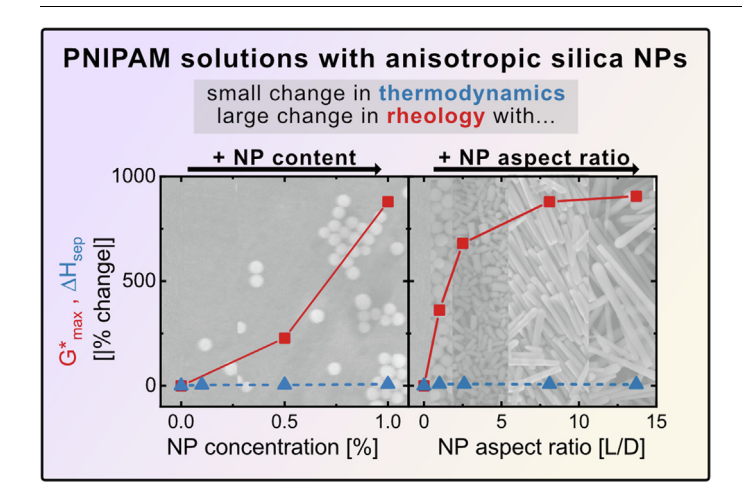


Tuning the thermodynamic, optical, and rheological properties of thermoresponsive polymer solutions via silica nanoparticle shape and concentration



Christopher A.P. Neal ^a, Valeria León ^b, Michelle C. Quan ^a, Nondumiso O. Chibambo ^a, Michelle A. Calabrese ^{a,*}

G R A P H I C A L A B S T R A C T



ARTICLE INFO

Article history:
Received 25 May 2022
Revised 12 August 2022
Accepted 22 August 2022
Available online 12 September 2022

Keywords.

Poly(N-isopropyl acrylamide) Lower critical solution temperature Silica nanospheres/nanorods Differential scanning calorimetry

ABSTRACT

Hypothesis: The shape and quantity of hydrophilic silica nanoparticles (NPs) can be used to tune the microstructure, rheology, and stability of phase-separating polymer solutions. In thermoresponsive polymer systems, silica nanospheres are well-studied whereas anisotropic NPs have little literature precedent. Here, we hypothesize that NP shape and concentration lower the onset of rheological and turbidimetric transitions of aqueous poly(N-isopropyl acrylamide) (PNIPAM) solutions.

Experiments: Differential scanning calorimetry (DSC), Fourier-transform infrared spectroscopy (FTIR), turbidimetry, and oscillatory rheology are utilized to examine interactions between NPs, PNIPAM, and water and to track changes in phase separation and rheological properties due to NP concentration and shape.

Findings: NP addition reduces phase separation enthalpy due to PNIPAM-NP hydrogen bonding

E-mail address: mcalab@umn.edu (M.A. Calabrese).

^a Department of Chemical Engineering and Materials Science, University of Minnesota Twin Cities, Minneapolis, MN 55455, United States

^b Mechanical Engineering Department, The University of Texas Rio Grande Valley, Edinburg, TX 78539, United States

Abbreviations: NP, nanoparticles; PNIPAM, poly(N-isopropyl acrylamide); DSC, differential scanning calorimetry; FTIR, Fourier-transform infrared spectroscopy; P87, number-average molecular weight 87 kDa PNIPAM; P310, number-average molecular weight 310 kDa PNIPAM; T_{low} , low-temperature beginning of phase separation; T_{on} , onset temperature; T_{inf} , inflection temperature of phase separation; T_{high} , high-temperature end of phase separation; T_{tr} , primary rheological transition temperature of solution.

^{*} Corresponding author.

Rheology Hydrogel Turbidimetry Fourier-transform infrared spectroscopy interactions, the degree to which depends on polymer content. While NP addition minorly impacts thermodynamic and optical properties, rheological transitions and associated rheological properties are dramatically altered with increasing temperature, and depend on NP quantity, shape, and polymer molecular weight. Thus NP content and shape can be used to finely tune transition temperatures and mechanical properties for applications in stimuli-responsive materials.

© 2022 Elsevier Inc. All rights reserved.

1. Introduction

Stimuli-responsive 'smart' materials that can actively respond to external fields and vary their micro- or nano-structure in realtime are foundational to future technologies in flexible displays [1–3], biosensors [4], organic light emitting diodes [5,6] and thin film photo-responsive cells [7–9]. These structural responses can lead to significant enhancements in physical properties such as optical reflectance [10-12], thermal or electrical conductivities [13–15], or mechanical strength [14,15], opening the door to increasingly complex applications. Thermoresponsive polymer solutions are one example of responsive materials that display dramatic microstructural responses with temperature change. Polymers that exhibit a lower critical solution temperature (LCST) undergo a conformational change due to worsened solubility with increasing temperature. Above this demixing temperature, macroscopic phase separation occurs. One of the most thoroughly investigated thermoresponsive polymer solutions is aqueous poly(Nisopropyl acrylamide) (PNIPAM) [16] which has an LCST near body temperature (~32 °C, dependent on polymer properties) making PNIPAM of interest for biomaterial and drug delivery applications

When aqueous PNIPAM solutions are heated above their phase separation temperature, the PNIPAM chains dehydrate and liberate bound water molecules [21]. Dehydration leads to a significant decrease in polymer hydrodynamic volume and causes chains to collapse into mesoglobules, decreasing conformational entropy [21,22]. This change in conformational entropy contributes to the heat input required to phase separate and can be quantified by differential scanning calorimetry (DSC) through the demixing enthalpy, ΔH_{sep} [21]. The thermodynamics of demixing can be controlled by altering the mechanism of polymer aggregation, such as by introducing preferential initiation sites or controlling the liberation of water molecules [23,24].

The resulting rheological behavior of phase-separating PNIPAM solutions depends highly upon PNIPAM concentration, molecular weight and end group chemistry. At low concentrations, collapsed PNIPAM chains aggregate into sparsely populated mesoglobules which can absorb light but generally do not cause an increase in dynamic moduli; mesoglobules are commonly seen at concentrations below 10^{-4} g/mL PNIPAM [22,25–28]. With increasing PNIPAM content, mesoglobules grow into larger flocks and then form space-filling aggregates above $\sim 10^{-3}$ g/mL; above the onset of phase separation, these flocks increase the dynamic moduli with increasing temperature due to hydrophilic interactions between flocks [22,26,28,29]. At significantly higher concentrations ($\geqslant 10^{-2}$ g/mL PNIPAM), flocks coarsen throughout the solution space, dramatically contracting and forming a strong hydrogel [22,25,29].

Adding nanoparticles (NPs) to thermoresponsive polymer solutions can alter rheological behavior and macroscopic properties of interest in applications including drug delivery, hydrogel formation and optically-tunable systems [30–35]. For example, PNIPAM-grafted mesoporous silica NPs can be used for targeted drug delivery due to the combination of particle porosity and

PNIPAM thermoresponsivity. At low temperatures, the grafted-PNIPAM chains swell, enabling small molecules to percolate into the NP pores; PNIPAM dehydration and subsequent collapse upon heating subsequently traps the small molecules [36-44,34]. Interactions between silica NPs and non-grafted PNIPAM have also been shown to control the temperature and mechanism of phase separation [45-47]. The presence of surface silanol (Si-OH) and siloxane (Si-O-Si) groups allow for substantial hydrogen bonding with hydrophilic PNIPAM amide groups, whereas hydrophobic van der Waals interactions form between silicon atoms and the hydrophobic portions of the PNIPAM backbone and isopropyl groups [45-47]. Petit et al. showed that the hydrophilic interactions between dilute PNIPAM (0.5% wt) and silica nanospheres decreased the enthalpy of phase separation yet broadened the temperature range of the transition due to colloidal stabilization [48]. PNIPAM chains interacting with NPs form fewer hydrogen bonds with surrounding water molecules and thus require less water liberation and less conformational change upon thermal phase separation than non-interacting PNI-PAM; as such, PNIPAM-NP interactions also decrease the entropic penalty to separation [48,49]. Due to these interactions, the PNIPAM separation preference varies with the inclusion of spherical silica NPs, improving mechanical strength and swelling and decreasing the phase separation temperature [50-57]. Zhao et al. [50] suggests that PNIPAM-NP hydrogen bonds act like brick and mortar, significantly increasing structural integrity of resulting structures by providing preferential H-bond bridges between PNIPAM mesoglobules and NPs. Weak attractive depletion forces between silica NPs in the presence of unbound neutrally-charged polymers like PNIPAM also decrease the interparticle distance and create polymer 'bridges' between NPs which aid in thermal aggregation [58] and are partially responsible for the increase in structural integrity of these mixtures [59,60]. However, steric repulsion between NPs due to the adsorbed polymer layer prevents widespread aggregation in good solvent conditions. Thus, the inclusion of silica NPs can both control the dynamic moduli of PNIPAM solutions for structural applications and the separation for thermally-active applications.

Utilizing structurally-anisotropic NPs in place of spherical NPs can expand the range of higher-order structures that can form without requiring high volume fraction suspensions, as is typically necessary for isotropic nanospheres [32,61,62]. Yadav et al. [63] recently showed that 0.1 nM gold nanospheres increase the phase separation temperature of PNIPAM solutions by 2 °C [64]. However, the same amount of gold nanorods with an aspect ratio of 3.2 increased the phase separation temperature by nearly 24 °C [64]. The authors hypothesize that hydrophobic NP-PNIPAM interactions effectively hide the hydrophobic side group regions while exposing amide groups to hydrogen bonding with water, stabilizing PNIPAM in solution [64]. Due to anisotropic surface properties of gold nanorods compared to isotropic surface properties of gold nanospheres, rods showed significantly higher increase in phase separation temperature over spheres [63]. While gold NP addition prevents PNIPAM-NP hydrogen bonding interactions, many thermosensitive applications require such interactions between PNIPAM amide groups and NPs so that a strong polymer-NP network forms [65,50].

As the introduction of silica NPs [50-57,66] and use of anisotropic NPs [64,63] can both have dramatic impacts on phase separation, combining these factors has the potential to yield further synergies leading to thermally-tunable mechanical and optical properties of PNIPAM solutions. However to our knowledge, no study has examined the role of silica NP aspect ratio on the thermoresponsiveness of PNIPAM solutions in which significant hydrogen bonding interactions occur between NPs and PNIPAM amide groups. To bridge this knowledge gap, we investigate the impact of hydrophilic [67-69] silica NP addition on phase separation thermodynamics, optical properties, and rheological transitions of aqueous PNIPAM solutions. These behaviors are examined across a range of polymer-NP solutions to uncover the synergistic and antagonistic effects from NP aspect ratio, NP concentration, polymer concentration, and polymer molecular weight. Here, silica NPs are chosen as a model system due to their hydrophilic surface and well-established synthetic procedure [68,67]. Phase separation temperatures are characterized via a combination of optical and rheological techniques including turbidimetry and rheology; thermodynamic quantities governing phase separation, such as enthalpy of demixing, are measured via differential scanning calorimetry (DSC). Changes in the phase separation behavior with NP addition are rationalized with Fourier transform infrared spectroscopy (FTIR) measurements of relative changes in interaction modes. These studies reveal fundamental insight into interactions between aqueous PNIPAM and anisotropic hydrophilic NPs, and outline how macroscopic mechanical properties and rheological transitions can be tuned via NP concentration, NP aspect ratio, and polymer molecular weight.

2. Methodology

2.1. Materials

Ethanethiol (97%), potassium phosphate, tribasic (reagent grade), acetone (>99.9%), 2-bromoisobutyric acid (98.0%), nhexane (>95%), ethyl acetate (>99.5%), silica gel (70-230 mesh), 1,4-dioxane (>99.0%), hexanes, mixture of isomers (>98.5%), methanol (>99.8%), and sodium citrate dihydrate (>99%) were used as received from Sigma-Aldrich. Carbon disulfide (99.9%), diethyl ether (99%, stabilized), 1-pentanol (99%) and tetraethyl orthosilicate (98%) were used as received from Acros Organics. Dichloro- methane (DCM, >99.5%) and sodium sulfate (>99.0%) were used as received from Macron Fine Chemicals. Hydrochloric acid (VWR, 36.5% - 38.0%) and tetrahydrofuran (Fisher scientific, >95%, stabilized), were used as received. Poly(vinyl pyrrolidone) (Alfa Aesar, 40 kDa, powder), ethanol (Pharmco-Aaper, 200 proof), and ammonia (Supelco, 25% (v/v)) were used as received. 2,2'-Azo bis(2-methylpropionitrile) (AIBN, Sigma-Aldrich, 98%) was recrystallized three times in methanol, vacuum dried and subsequently stored in a flammable freezer. N-isopropyl acrylamide (NIPAM, Fisher scientific, 98.0%, stabilized) was purified via sublimation. The chain transfer agent (CTA) for RAFT polymerization was 2-(et hylsulfanylthio-carbonylsulfanyl)-2-methylpropionic acid (EMP); for synthesis details and NMR spectra, see SI.2.1-SI.2.2. High molecular weight poly(N-isopropyl acrylamide) ($M_n \sim 314$ kDa; $D\sim 3.03$) was used as received from Scientific Polymer Products; for NMR and SEC characterization, see SI.2.2 and SI.3, respectively.

2.2. Synthesis of linear PNIPAM

NIPAM (12.5 g, 110 mmol, 1105 equiv.), EMP (22.5 mg, 0.1 mmol, 1 equiv.), and AIBN (1.65 mg, 0.01 mmol, 0.1 equiv.)

were dissolved in 54 mL of 1,4-dioxane and degassed via three freeze-pump-thaw cycles down to a maximum of 25 mTorr. The flask was backfilled with nitrogen, brought into a 70 °C oil bath for 18 h, and then quenched in liquid nitrogen and exposed to oxygen. Purification followed three subsequent dissolutions using the minimum amount of THF and precipitations in cold hexanes: diethyl ether (3:2) and then vacuum dried overnight at 40 °C. Resulting polymer had an $M_n \sim 87$ kDa and $\Phi \sim 1.43$ (see SI.2.2 for NMR and SI.3 for SEC) and is referred to as P87.

2.3. Silica NP synthesis and purification

In this work, silica nanoparticles are referred to as NP unless otherwise stated. Bare silica NPs with aspect ratios, A, of 2.5, 8, and 14 (designated A2.5, A8, and A14) were synthesized following prior protocols [67.69]. This synthetic method produces NPs of approximately constant diameter; thus aspect ratio was primarily altered via NP length. In short, 30 g of poly(vinyl pyrrolidone), 300 mL of 1-pentanol, 30 mL ethanol, 8.4 mL deionized water, 2 mL of 0.18 M sodium citrate in water, and 6 mL of 25% (v/v) ammonia were mixed with a combination of vortexing and sonication. Finally, TEOS was added last; for A2.5, A8 and A14 NPs, 1.5, 4.5 and 7.5 mL TEOS were used, respectively. For A8 batches, TEOS was added in two equal additions spaced 6 h apart. For A14 NPs, 3 mL TEOS was added, followed by 3 mL after 6 h and 1.5 mL after 18 h. Following each TEOS addition, reactors were gently swirled for 10 s to mix. Bare silica nanospheres (A1) were synthesized following protocols by Bogush et al. [70]. Here, 20 mL ammonia solution (0.714 M NH₃, 25% (v/v)), 1.2 mL water (2.99 M H₂O) and 230 mL ethanol were mixed in an HDPE bottle. Under light mixing, 11.3 mL TEOS (0.17 M TEOS) was added rapidly for a target diameter of 275 nm [70].

Approximately 18 h after initiation, NPs were purified through an extensive centrifugation protocol (see SI.5). NPs were then dried at 50 °C under vacuum overnight, ground with a mortar and pestle, and calcined in air at 500 °C for 5 h to remove residual polymer and organic compounds.

2.4. Silica NP characterization

2.4.1. Scanning electron microscopy (SEM)

NP dimensions are characterized using a JEOL 6010 scanning electron microscope at 5 kV; select images are shown in Fig. 1 (see SI.6.1 for more images). For explanation of NP endcap shape, see SI.9. Particle dimensions were analyzed using ImageJ software to quantify length, diameter and aspect ratio (A = L/D); ~100 NPs were analyzed per batch to provide statistical distributions (SI.6). Aspect ratios (A = L/D) of NPs were 2.6 ($L = 730 \pm 27$ nm; $D = 285 \pm 12$ nm, Fig. 1b), 8.1 ($L = 2500 \pm 110$ nm; $D = 310 \pm 9$ nm, Fig. 1c) and 13.7 ($L = 6450 \pm 290$ nm; $D = 470 \pm 20$ nm, Fig. 1d), denoted A2.5, A8, and A14. Nanospheres ($L = D = 275 \pm 25$ nm, Fig. 1a) are denoted A1. Although some large outliers are visible for A2.5 (Fig. 1), the majority of NPs are nearly homogeneous in size and shape, producing a fairly low dispersity (see SI.6). Note that A14 NPs are thicker than other NPs, which is accounted for in data analysis.

2.4.2. BET Surface area analysis

BET method characterized specific surface area (m^2/g) of A1 and A8 NPs for comparison of synthesis methods. Physisorption was performed on an ASAP Micrometrics 2020 analyzer using N_2 as the adsorbate. See SI.6.2 for surface roughness and SI.6.5 for pore surface area characterization using BET results.

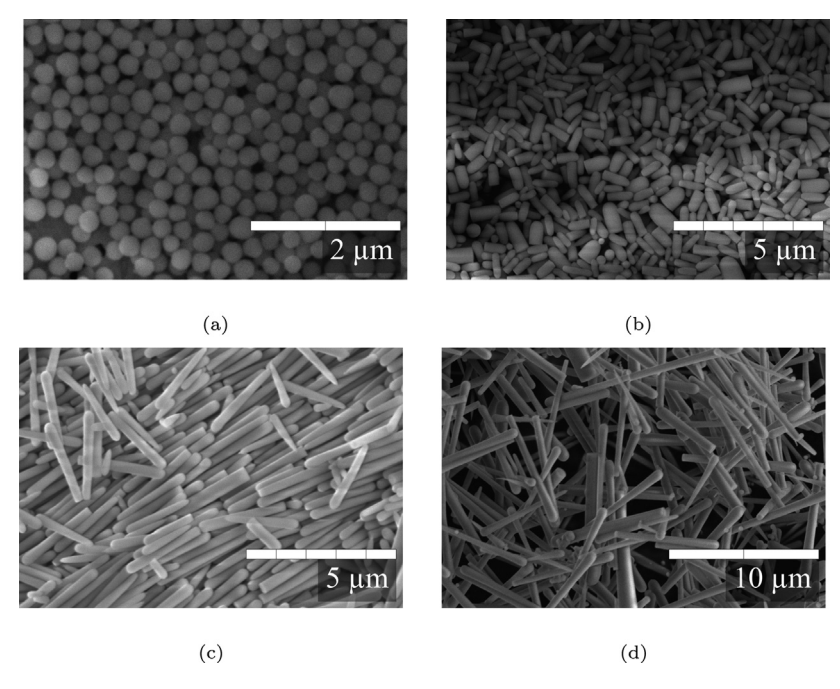


Fig. 1. SEM images of silica (a) nanospheres (A1) and (b-d) nanorods with aspect ratio (b) A2.5 (1.5 mL TEOS/batch), (c) A8 (4.5 mL TEOS/batch) and (d) A14 (7.5 mL TEOS/batch). To accurately demonstrate sizes and changes in nanorod anisotropy, magnification varies between images. See SI.6.1 for more images and similar magnifications.

2.4.3. DLS analysis

The hydrodynamic radii, R_h , and ζ -potentials were quantified using a Malvern Zetasizer dynamic light scattering (DLS) instrument. Hydrodynamic radius of PNIPAM was quantified in poly (methyl methacrylate) (PMMA) semi-micro cuvettes filled with at least 0.8 mL of 10 mg/mL polymer solution; radii were confirmed with 1 mg/mL solutions. ζ -potential was quantified in disposable folded capillary cells using the Smoluchowski equation, $\zeta = \eta U/\epsilon$, where U is the electrophoretic mobility, ϵ is the electric permitivity of the medium, and η is the viscosity of the medium. Scattering was collected at 25 °C in HPLC grade water through triplicates of 11 scans of 10 s each. The R_h for P87 and P310 are 11 nm and 23 nm, respectively; see SI.3.1 for explanations of uncertainties. ζ -potential values for A1, A2.5, A8, and A14 NPs are -34 ± 1 mV, -40 ± 1 mV, -47 ± 1 mV, and -49 ± 2 mV, respectively.

2.4.4. Surface silanol density estimation

Surface silanol (Si-OH) density of NPs was estimated utilizing a combination of BET theory and thermogravimetric analysis (TGA) [71]. Mass as a function of temperature was quantified from 25 °C to 1000 °C at a rate of 10 °C/min on a Mettler Toledo TGA/DSC 1 STAR System. Utilizing the Zhuravlev method (see SI.6.4) [71], mass loss from 180 °C to 1000 °C was converted into surface silanol density. Surface silanol analysis of A2.5 NPs could not be done due to insufficient sample quantity. Surface silanol densities of A1, A8, and A14 NPs were 3.8, 12, and 11 OH/nm², respectively, using the surface area measured in BET; see SI.6.4 for additional details and calculations.

2.5. Polymer-NP solution preparation

Aqueous polymer-NP solutions targeted three NP contents (0.1%, 0.5%, 1.0%) for four NP aspect ratios (A = 1, 2.5, 8, 14) and two polymer contents (2%, and 6%); all % are by mass. For each NP aspect ratio, solutions were also made at 0.5% P87 and five NP contents (1%, 2%, 3%, 4%, 5%). Recipes for each batch are shown in SI.7. Solutions are abbreviated with x% Pm/ y% Az, where x is polymer content (in %), y is silica content (in %), and z is NP aspect

ratio. Polymer number average molecular weight is denoted by m with either 310 or 87 (for 310 kDa and 87 kDa, respectively). For example, 2% P310/0.1% A8 refers to 2.0% 310 kDa polymer and 0.1% aspect ratio eight NPs. For each solution, the appropriate amount of dry NP, dry polymer, and HPLC grade water were added to a 2 dram vial. Vials were capped and shaken for \sim 1 min and sonicated under ice for \sim 6 h to break up aggregates. Solutions were then refrigerated and shaken for \gg 4 days. To counteract potential settling, solutions were vortexed for \sim 30 s and sonicated for 5 s immediately before use.

2.6. Differential scanning calorimetry (DSC)

Differential scanning calorimetry (DSC) measured heat flow as a function of temperature using a TA Instruments DSC Q2000 and hermetically-sealed aluminum Tzero pans. Pans ($\sim\!\!20~\mu L$) were loaded at 20 °C and equilibrated for 1 min. Temperature was increased from 20 °C to 50 °C at 1 °C/min. DSC temperature ramps were also collected for select solutions at 0.2 °C/min (S15) to allow for direct comparison to rheological studies at 0.2 °C/min; however, these trials were only used qualitatively due to low signal. A Python code was written to determine an appropriate baseline following the tangential sigmoidal baseline model (TA Instruments Universal Analysis); for equation and constraints, see SI.20. The integral of phase separation peaks results in an enthalpy of separation that can be normalized to the mass of solution (J/gsample) and then further to the moles of NIPAM monomers in the polymer chain (kJ/mol_NIPAM) (shaded area of Fig. 2a).

2.7. Vibrational spectroscopy

Fourier-transform infrared (FTIR) spectra were collected using a Thermo Nicolet 6700 spectrometer in attenuated total reflection (ATR) mode. Approximately 2 uL of solution was deposited onto the diamond crystal. 64 scans were collected for each solution from 650 cm $^{-1}$ to 4000 cm $^{-1}$ with a resolution of $\sim\!0.964$ cm $^{-1}$. Data was baseline-corrected via the Thermo Fisher software. For FTIR peaks and vibrational mode designations, see SI.19.

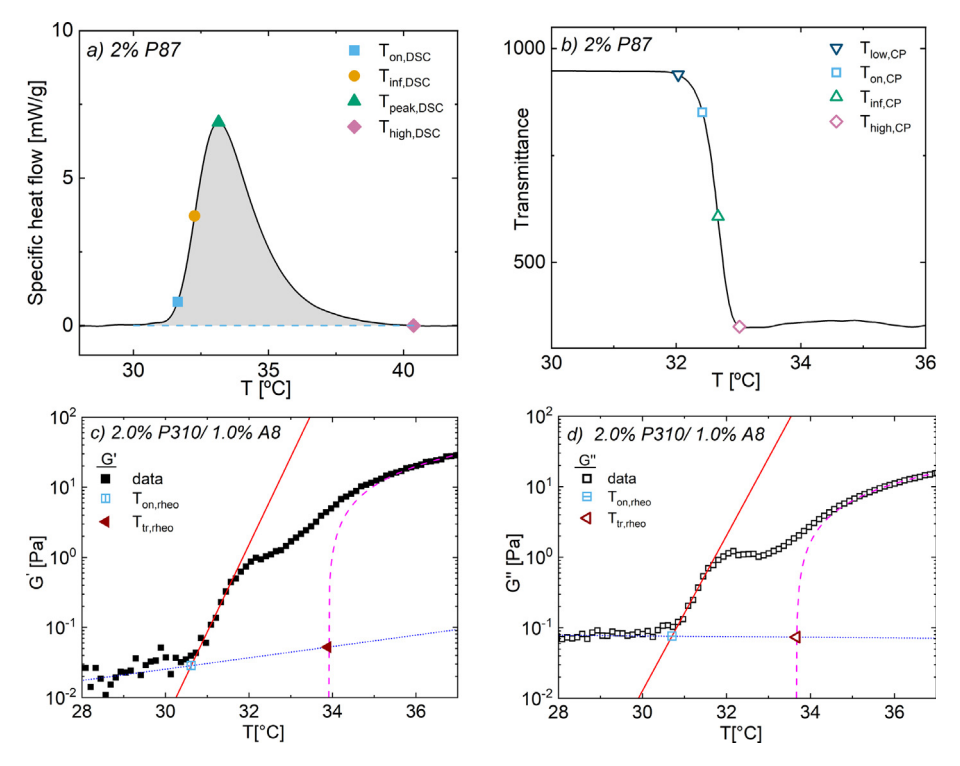


Fig. 2. (a) Baseline-subtracted heat flow (DSC), (b) transmittance as a function of temperature for 2% P87. (c) Storage and (d) loss moduli (rheology) as functions of temperature for a solution of 2% P310 and 1% A8 NPs in water. Heating rates are (a) 1 °C/min and (b), (c), and (d) 0.2 °C/min. Phase separation temperatures are overlaid. Tangents in (c) and (d) are drawn from low temperature moduli (T < 28 °C; blue, dotted), and the points of maximum slope on a semi-log-y plot (red, solid; through $T_{on,rheo}$) and a linear–linear plot (pink, dashed; through $T_{tr,theo}$). Note that straight lines drawn on a log-linear plot curve, as shown.

2.8. Turbidimetry

To determine optical transition temperatures associated with phase separation, $T_{x,CP}$, light transmittance was measured with increasing temperature using an in-house instrument (Fig. S16). An aluminum block was machined to include square holes for standard 4 mL 10 mm pathlength acrylate cuvettes. A red laser (5 mW, class 3R, 650 nm) and a standard CdS photoresistor detect changes in transmittance in real-time. A cartridge heater and PTD thermocouple control the temperature of the cell, and a Peltier module and CPU fan provide active cooling. All components were controlled by an Arduino Uno which recorded absorbance vs. temperature. Solutions were heated from 25 °C to 40 °C at 0.2 °C/min. To correct for reflectance and absorbance of light by NPs, transmittance data was normalized from the values at 30 °C and 40 °C (as Tr = 1.0 and Tr = 0, respectively) to minimize complications derived from NP absorption; see SI.18.

2.9. Oscillatory rheology temperature ramps

Polymer aggregation associated with phase separation induces a mechanical response [72,73] which was quantified via oscillatory rheological temperature ramps. Rheological behavior of PNIPAM-NP suspensions was analyzed using an Anton Paar MCR 302 rheometer and a 50 mm diameter cone-and-plate (1°) geometry. A temperature-controlled Peltier hood ensured temperature homogeneity. Solutions were pre-sheared at 10 s $^{-1}$ for 5 min and allowed to rest for 5 min at 20 °C. The linear viscoelastic (LVE) regime for solutions was determined using amplitude sweeps from 0.01 to 20% ($\omega=10~{\rm rad\cdot s}^{-1}$); the amplitude used was chosen as the maximum amplitude in the plateau region of the loss modulus versus amplitude ($log_{10}(G\prime\prime)$ vs. $log_{10}(\gamma)$). An amplitude of 1% was chosen for all solutions. See Sl.13 for examples of amplitude sweeps for 0% NPs solutions.

Temperature ramps were collected at $\gamma=1\%$ and $\omega=10$ rad·s⁻¹ from 20 °C to 40 °C at a rate of 0.2 °C/min (0.1 min/data point; 0.02 °C resolution). Supplementary experiments at $\gamma=0.1\%$ confirmed that shear did not have a large impact on phase separation (SI.15). Note that noisy data at low temperatures is attributed to low torque signals due to low viscosity. Due to low yield of A2.5 NPs, temperature ramps on 2% P310 with A2.5 NPs was not possible for this examination.

Rheological transition temperatures are quantified by the intersection of two lines, one in the low temperature region and one tangent to the maximum slope in dynamic moduli; this intersection is done for both G' and G'' (see Sl.16). For rheological data that includes shoulders or multiple transitions, the final transition leading to peak or plateau moduli denotes the main rheological transition temperature, $T_{tr,theo}$ (Fig. 2c, d).

2.10. Transition temperatures across techniques

As changes in any single transition temperature cannot fully describe changes in separation [16], multiple temperatures are defined for each technique. For DSC and turbidimetry, the temperature where the maximum change in signal–heat flow and transmittance, respectively–and thus the inflection of the derivative occurs is denoted as T_{inf} . To determine the onset temperature, T_{on} , the intersection temperature of tangents from T_{inf} and low-temperature data before the transition is used. For DSC, T_{peak} is the point of maximum heat flow following baseline–subtraction (which is similar to but not necessarily the same as T_{inf}) and T_{high} is the temperature such that the integration of heat flow changes at a rate lower than 0.2% per °C (see SI.21). For turbidimetry, T_{low} and T_{high} are the temperatures such that the derivative of transmittance as a function of temperature is 5% of the maximum value below and above T_{peak} , respectively. DSC heat flow and turbidimet-

ric traces, with phase separation temperatures overlayed, are shown in Fig. 2a and 2b.

Rheological transition temperatures are drawn from similar methods, though distinction from tangents drawn from G1, G11 vs T and logG₁, logG₁ vs. T should be noted. First, tangents are drawn from dynamic moduli vs temperature data below the transition temperatures (chosen as 25 to 30 °C, called the 'lowtemperature' region). Using linear dynamic moduli, the maximum slope is weighted towards higher temperatures of the phase separation and is usually attributed to polymer chain collapse and weak H-bonding network formation [72,73]; the intersection of a tangent drawn from the maximum slope of linear dynamic moduli and the low-temperature tangent is designated $T_{tr.rheo}$, or the temperature of primary transition (Fig. 2c and 2d). On a logarithmic axis, the inflection point is weighted towards lower temperatures (as moduli increase is weaker than exponential, on average); the intersection of a tangent drawn from the maximum slope of logarithmic dynamic moduli and the low-temperature tangent and is denoted $T_{on,rheo}$. Whereas $T_{tr,rheo}$ provides information on when larger-scale hydrogen-bonding networks form, Ton, rheo provides insight into microstructures formed during low-intermediate $(T < T_{tr})$ temperatures. See SI.16 for details.

2.11. Statistical analysis

Statistical significance of trends in quantified results (separation temperatures, enthalpies, etc.) was determined using a simple linear regression test through spreadsheet software internal calculations. For this work, both a p-value less than 0.05 and 95% confidence intervals are used as benchmarks to determine statistical significance of trends. See SI.30 for calculated p-values and 95% confidence intervals. In all tables in this work, uncertainty in parentheses is the standard error of the mean.

3. Results and discussion

3.1. Thermal signatures of phase separation in the presence of NPs

Thermal phase transitions in dilute solutions of 87 kDa PNIPAM, denoted 0.5% P87, depend on both NP concentration and aspect ratio (A) between A1 (spheres) and A14 (rods). Differential scanning calorimetry (DSC) quantified the phase separation enthalpy (ΔH_{sep}) and thermal transition temperatures ($T_{x,DSC}$, Fig. 2a) as a function of NP concentration and aspect ratio. These polymer and NP concentrations were selected for comparison with prior work by Petit et al. on PNIPAM/silica nanosphere solutions [48], albeit here the nanosphere diameter and PNIPAM molecular weight are both an order of magnitude larger (\sim 30 nm vs. \sim 300 nm, 8.5 kDa vs. 87 kDa, respectively). Additionally, the dilute polymer content allows for better understanding of PNIPAM-NP interactions in the absence of significant polymer–polymer interactions, prior to examining more concentrated polymer solutions in Section 3.3.

All PNIPAM/NP solutions examined in this work exhibit a single, broad endothermic peak in the heat flow trace corresponding to phase separation (Fig. 3a), regardless of NP content and aspect ratio; see SI.32 for raw DSC traces, and SI.29 for tabulated values. Here, $\Delta H_{\rm Sep}$ for bare PNIPAM solutions is ~50% greater than in Petit et al. (5.9 kJ/mol_NIPAM vs. 4.3 kJ/mol_NIPAM in [48]), likely due to differences in polymer end group and molecular weight [74,75]. As molecular weight of PNIPAM increases, enthalpy of transition also increases due to entropic penalties from entanglements preventing dehydration and collapse [74].

Increasing NP content linearly decreases the phase separation enthalpy in dilute P87 solutions for all aspect ratio NPs (Fig. 3b,

Table 1). For solutions with nanorods, the decrease in ΔH_{sep} is between 0.12 and 0.21 kJ/mol_{NIPAM} per % NP; hydrogen bonds between PNIPAM amide groups and NP silanols are likely responsible for the decrease in ΔH_{sep} [64,48,50–57]. NIPAM groups adsorbed onto the surface of silica NPs have fewer amides available to hydrogen bond with water molecules and a decreased potential for dehydration upon temperature increase; this hydrogen bonding interaction is illustrated in Fig. 4. Interestingly, while NP inclusion decreases ΔH_{sep} , the transition onset and peak temperatures measured via DSC, $T_{on,DSC}$ and $T_{peak,DSC}$, are independent of NP content (Table 1), in contrast to the increase in $T_{on,DSC}$ seen by Petit et al. [48]. However below 3% NP, these authors note only minimal shifts in $T_{on,DSC}$ [48]; when the differences in NP specific surface area are accounted for, expected polymer coverage here falls in the regime with little observed change in $T_{on,DSC}$.

The decrease in ΔH_{sep} with NP content in this work is weaker than the trend observed by Petit et al. with 30 nm silica nanospheres (\sim 0.36 kJ/mol_{NIPAM} per % NP) (pink \blacklozenge , Fig. 3b) [48], potentially due to the larger total NP surface area in Petit et al. [48]. As the nanospheres utilized by Petit et al. have a higher total surface area than the NPs used here, and the reduction in ΔH_{sep} with NP aspect ratio appears non-monotonic (m-values, Fig. 3), ΔH_{sep} was also normalized by the NP surface area for all aspect ratios to examine the impact of particle shape in the absence of surface area as a confounding variable (Fig. 5a). See SI.6.3 for details on surface area characterization and SI.22 for enthalpy normalization. After surface area normalization, nanospheres in this work actually decrease $\Delta H_{sep}/m_{NP}^2$ by threefold more than those in Petit et al. (SI.23). Interestingly, ΔH_{sep} per NP surface area decreases more rapidly (steeper slope in Fig. 5a) with increasing NP aspect ratio (Fig. 5b). Yadav et al. [64] previously showed a substantial impact of NP aspect ratio on the DSC phase transition shape, transition temperatures, and ΔH_{sep} in PNIPAM solutions with hydrophobic gold nanorods, which the authors attributed to PNIPAM stabilization on the hydrophobic curved portions of gold nanorods. However here, no significant change in either DSC peak shape or position occurs with NP addition. Additionally, the stronger decrease in $\Delta H_{sep}/NP$ surface area with increasing NP aspect ratio observed here likely cannot be explained by NP curvature, as differences in the polymer vs. NP size likely diminish curvature effects [76-78]. For example, the PNIPAM average hydrodynamic radius ($R_{h,P87}$ = 11 nm, $R_{h,P310}$ = 23 nm; see SI.3.1 for explanations of uncertainties) and silica NP radius ($R_{NP} \sim 150$ nm) substantially differ in this work, whereas both length scales are comparable in Yadav et al. $(R_{h,NP} \sim R_{g,PNIPAM} \sim 5 \text{nm})$ [64].

To better explain why $\Delta H_{sep}/NP$ surface area is influenced by NP aspect ratio, NP surface properties and colloidal stability were examined via ζ-potential. As shown in Fig. 5b, NP ζ-potential is negative for all NP solutions, with more negative values with increasing NP aspect ratio indicating improved stability due to more significant electrostatic repulsive forces. The ζ-potential and $\Delta H_{sep}/m_{NP}^2$ scale similarly with NP aspect ratio, suggesting that this aspect ratio effect is largely due to differences in NP ζpotential. Colloidal silica solutions are known to exhibit a higher stability to aggregation, i.e. greater magnitude ζ-potentials, than predicted by classical Derjaguin-Landau and Verwey-Overbeek (DLVO) theory [79–82] which considers the total interaction energy between two particles as the sum of van der Waals attractions and electrostatic double layer repulsions. This enhanced stability is generally attributed to an additional repulsive force resulting from the presence of hydroxyl groups on the NP surface, which introduce sites for hydrogen bonding with water [83,84,71,85-88]. This shortrange repulsive force is generally explained as a repulsive hydration force [79,84,81] or as a polymer-like steric repulsion that results from the protruding surface groups [82].

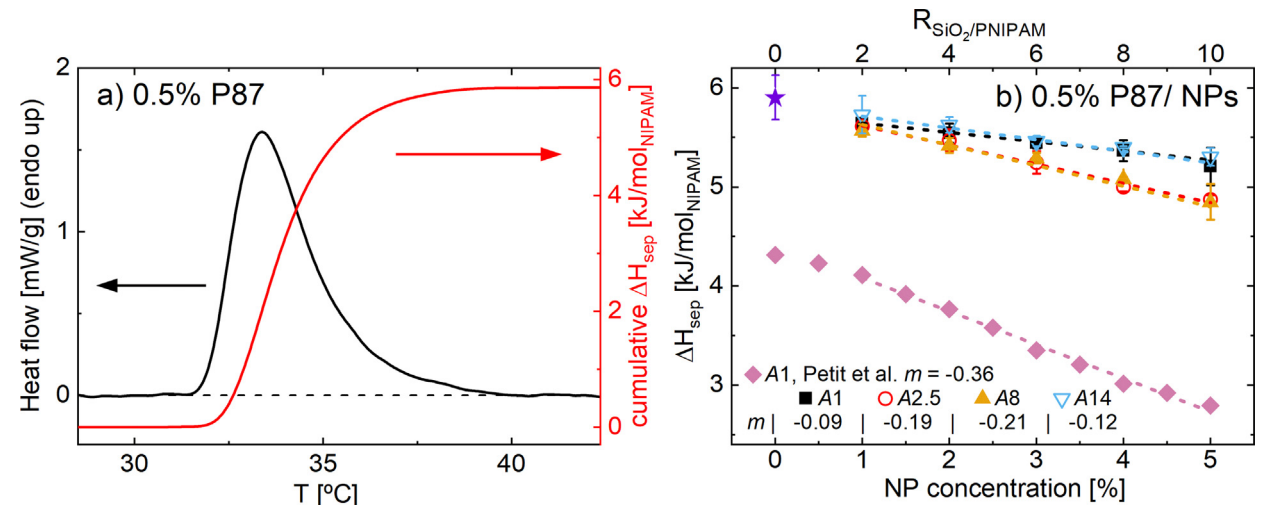


Fig. 3. a) Specific heat flow and cumulative separation enthalpy for 0.5% P87. b) Separation enthalpy, ΔH_{sep} , as a function of NP content. Data digitized from Petit et al. [48] on shorter PNIPAM (M_n = 8.5 kDa) and smaller nanospheres (R = 15 nm) is shown for comparison. ΔH_{sep} decreases roughly linearly with increasing NP content in most cases, following a similar scaling. Error bars are mean standard error ($N \ge 3$); m denotes slope of linear fits in kJ/mol_{NIPAM} per % NP. Note that A14 NP data is shifted slightly upward from data for A2.5 and A8 NPs, likely due to changes in surface area; see Fig. 5 which accounts for this change.

Table 1 Phase separation onset $(T_{on,DSC})$, peak heat flow $(T_{peak,DSC})$ temperatures and phase separation enthalpy (ΔH_{sep}) as derived from DSC for solutions of 0.5% P87.

NP inclusion	$T_{on,DSC}$ [${}^{\underline{o}}$ C]	$T_{peak,DSC}$ [${}^{\circ}$ C]	ΔH_{sep} [kJ/mol _{NIPAM}]
2% P87			
0%	31.93 (0.02)	33.35 (0.03)	5.90 (0.22)
1% A8	32.02 (0.05)	33.47 (0.04)	5.57 (0.06)
2% A8	31.96 (0.01)	33.40 (0.01)	5.42 (0.08)
3% A8	32.00 (0.01)	33.42 (0.02)	5.29 (0.05)
4% A8	31.97 (0.02)	33.42 (0.02)	5.08 (0.02)
5% A8	32.04 (0.03)	33.44 (0.02)	4.85 (0.18)
5% A1	31.81 (0.07)	33.20 (0.06)	5.21 (0.19)
5% A2.5	32.04 (0.05)	33.53 (0.04)	4.87 (0.04)
5% A14	31.95 (0.01)	33.40 (0.01)	5.14 (0.05)

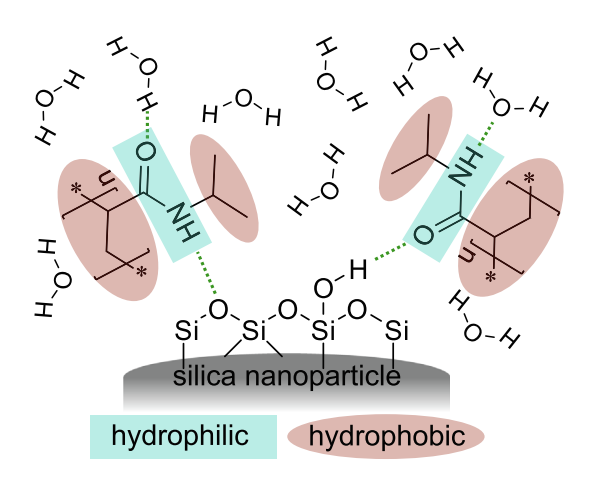
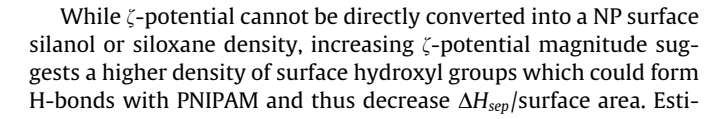


Fig. 4. Schematic of hydrogen bonding (dotted green lines) between NP surface silanol/siloxane groups and water or PNIPAM. PNIPAM-NP associations partially dehydrate PNIPAM prior to phase separation, explaining the negative trend between ΔH_{sep} and NP content in Fig. 3. Note: NP surface curvature not drawn to scale



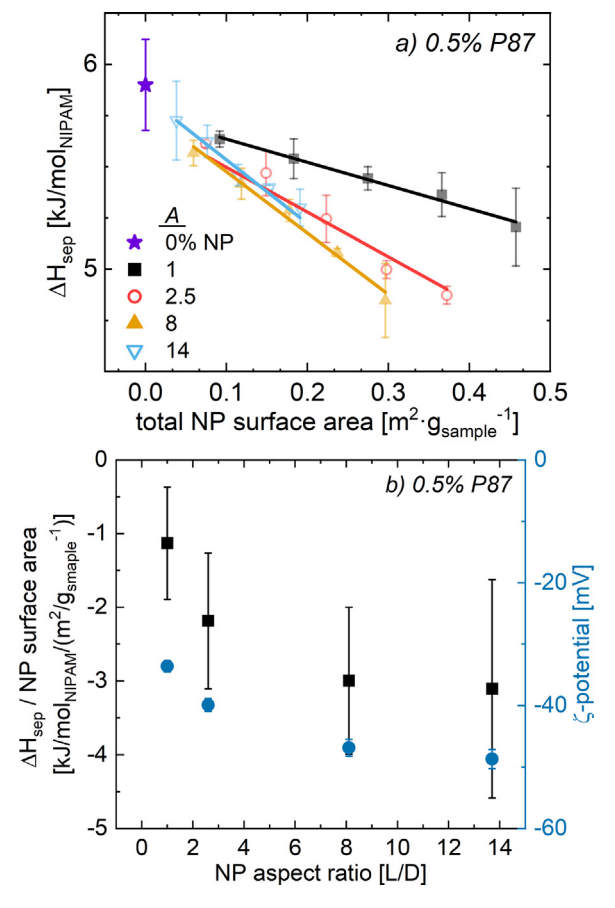


Fig. 5. (a) DSC separation enthalpy, ΔH_{sep} , of 0.5% P87 with NPs in water. NP content is normalized using the specific surface area, m²/g, of each A of NP found using SEM images in Fig. 1. (b) Slopes of ΔH_{sep} with NP content of trendlines shown in (a), as well as ζ -potential as a function of NP aspect ratio.

mates of the surface silanol density, δ_{OH} , using the Zhuravlev method [71] confirm that these differences in ζ -potential can be attributed in part to an increasing δ_{OH} with increasing NP aspect ratio (see Sections 2.4.4, SI.6.4). These measurements support the

link between ζ -potential and ΔH_{sep} /surface area: more surface OH groups both stabilize suspended NPs while also promoting more polymer-NP interactions, making the ζ -potential more negative and decreasing ΔH_{sep} /surface area more substantially for higher A NPs with higher δ_{OH} .

Interestingly, while Yadav et al. [64] attributed aspect ratio effects to NP curvature, the authors similarly note a larger ζ -potential magnitude in nanorods vs. nanospheres, which could also contribute to the reported behavior. Comparison of ΔH_{sep} changes and NP ζ -potential in Fig. 5b thus suggests that the ability for NPs to depress phase separation enthalpy is due to a combination of total NP surface area and surface charge. This combined effect may also explain the differences in ΔH_{sep} reduction with nanosphere addition in this work vs. Petit et al. [48], though thorough surface characterization was not reported in their work.

While NP addition decreases ΔH_{sep} , if the proposed mechanism is correct, few polymer-solvent H-bonds are disrupted with NP addition. To contextualize the magnitude of the decrease in ΔH_{sep} with NPs, the PNIPAM-water hydrogen bonding interactions are considered, where each monomer can form a maximum of three 'direct' hydrogen bonds from the amide group when fully hydrated - one from the amine (H-bond donor) and two from the carbonyl (H-bond acceptor) [21,89,90]. Additional water molecules form a hydration shell around the monomer, known as hydrophobic hydration [21,91]. Here, separation enthalpies in Fig. 3b are per monomer unit (4-6 kJ/mol_{NIPAM}) and are significantly smaller than the magnitude of the H-bond formation enthalpy between an amide group and water ($\sim 50 \pm 15 \text{ kJ/mol}_{H-bond}$) [91–93] or between two water molecules ($\sim 10 \text{ kJ/mol}_{H-bond}$) [91,94]. However, ~2/3 of direct PNIPAM-water hydrogen bonds survive the thermal phase separation transition [91,89,95,96], and approximately two waters from the hydrophobic hydration shell are released to the bulk during phase separation [21,91]. During phase separation new PNIPAM-PNIPAM H-bonds also form [89,91,95], but the number of new amide-amide bonds per monomer is low (<one per ten monomers) [91]. Thus, a relatively low ΔH_{sep} is due to the small number of disrupted polymer-solvent H-bonds from NP addition and a balance between liberating one directlybound water molecule and the formation of bulk water H-bonds by the two waters per monomer released from the hydrophobic hydration shell [91].

3.2. Spectroscopic signatures of polymer-NP interactions

Vibrational spectra of the dilute P87/NP solutions at ambient conditions (Fig. 6) provide additional evidence for the polymer-NP interaction mechanism (Fig. 4), as interactions in solution are altered at temperatures far below the onset of phase separation. Increasing either the NP concentration or aspect ratio has a similar impact on spectroscopic signatures of hydrogen bonding interactions in solution (Fig. 6); see SI.37 for complete set of spectra across NP aspect ratio and concentration. As solutions are dilute in polymer relative to other components, FTIR spectra are dominated by water and silica signals; thus polymer-particle interaction modes are examined via differences in hydrogen bonding between water molecules and between water and PNIPAM. For peak assignments and more in-depth analysis of FTIR peak intensity changes, see SI.24 and SI.26.

Changes in vibrational spectra with increasing NP content (Fig. 6a) and aspect ratio (Fig. 6b) occur in three main regions: water-water hydrogen bonding ($\sim\!\!3300~{\rm cm}^{-1}$), PNIPAM-water hydrogen bonding ($\sim\!\!1630~{\rm cm}^{-1}$), and silica intra-particle modes ($\sim\!\!1100~{\rm cm}^{-1}$). Water-water hydrogen bonding modes around 3300 cm $^{-1}$ and PNIPAM-water hydrogen bonding modes around 1630 cm $^{-1}$ provide insight into hydration shells around NIPAM

groups and the affinity of polymer–solvent interactions. Increases in overall intensity of modes from 750 cm⁻¹ to 1300 cm⁻¹ with increasing NP content (Fig. 6a) are attributed to various stretching and bending modes from the NPs, such as asymmetric Si-O bond vibration (1090 cm⁻¹), asymmetric vibration of Si-OH (950 cm⁻¹), and symmetric vibration of Si-O (795 cm⁻¹) [97]. Although silica modes in this region can qualitatively determine differences in silica concentration and NP surface hydrophilic groups, changes in the modes around 1100 cm⁻¹ were not further evaluated due to the convolution of several vibrational modes.

Water-water hydrogen bonding modes between 3000 cm⁻¹ and 3700 cm⁻¹ decrease in intensity with increasing NP concentration (Fig. 6a,c) and NP aspect ratio (Fig. 6b,d). To better demonstrate relative changes in intensity, the water hydrogen bonding region of the FTIR spectra in Fig. 6a and b are shown in Fig. 6c and d, subtracting data from (c) 0% NPs and (d) 5% A1 NPs; these modes are compared only semi-quantitatively, as without Raman spectroscopy, thorough peak deconvolution is difficult for aqueous solutions [98]. Peak intensities in the lower wavenumber water modes ($v < 3450 \text{ cm}^{-1}$) corresponding to single-donor, doubleacceptor (DAA, 3004 cm⁻¹), double-donor, double acceptor (DDAA, 3200 cm⁻¹), and single-donor, single-acceptor (DA, 3440 cm⁻¹) OH-bending modes decrease with increasing NP concentration (Fig. 6c); the number of 'donors' is the number of H-bonds from the hydrogen atoms in a water molecule whereas the number of 'acceptors' is the number of H-bonds from the oxygen atom (see SI.25).

This decrease in intensity of several water hydrogen bonding modes is unsurprising given that the presence of NPs breaks up the extensively coordinated bulk hydrogen bonding network [89,90]. Prior to phase separation, the amide group on PNIPAM serves as an initiation site for extensively H-bonded water clusters with high concentrations of DDAA bonding; these clusters partially break up during PNIPAM phase separation and decrease the average number of H-bonds per water molecule [89,90]. With amide groups and silica NPs associating, initiation sites for such 'solid' water clusters decrease in number causing a decreased intensity in the DDAA FTIR peak. This breakup of DDAA hydrogen bonding is present both with increasing NP concentration (Fig. 6e) and increasing aspect ratio (Fig. 6f). One possible explanation is that longer NPs extend a farther distance in solution and disrupt a larger portion of the bulk hydrogen bonding network than smaller NPs. The disruption of DDAA clusters with increasing NP aspect ratio could also relate back to longer NPs having higher ζpotential (Fig. 5b) such that NP surface charge is felt further from the NP surface, disrupting a higher number of clusters. As a result, further water cluster disruption during PNIPAM phase separation is limited in NP solutions, lowering the required energy input (Fig. 3).

Increasing NP content (A8, Fig. 6e) or NP aspect ratio (Fig. 6f) decreases the intensity of the peak around 1630 cm⁻¹. The main contribution to this peak is PNIPAM amide C=O stretching due to hydrogen bonding with water, though contributions from H₂O scissoring and the surface hydroxyl groups of mesoporous silica are also present [99]. Following PNIPAM-silica hydrogen bonding interactions, the hydrophobic PNIPAM backbone and isopropyl groups are exposed to the bulk of the solvent and exclude some water from the hydration shell around the amide. A decrease in this amide-water H-bonding portion of the 1630 cm⁻¹ peak corresponds to a decrease in the overall polymer-solvent hydrogen bonding strength [100-102], suggesting that NPs disrupt polymer-solvent hydrogen bonds at room temperature. Thus as NP concentration increases, fewer H-bonds between PNIPAM and water are present which must be broken to dehydrate the polymer, in agreement with DSC findings that NP addition reduces ΔH_{sep} .

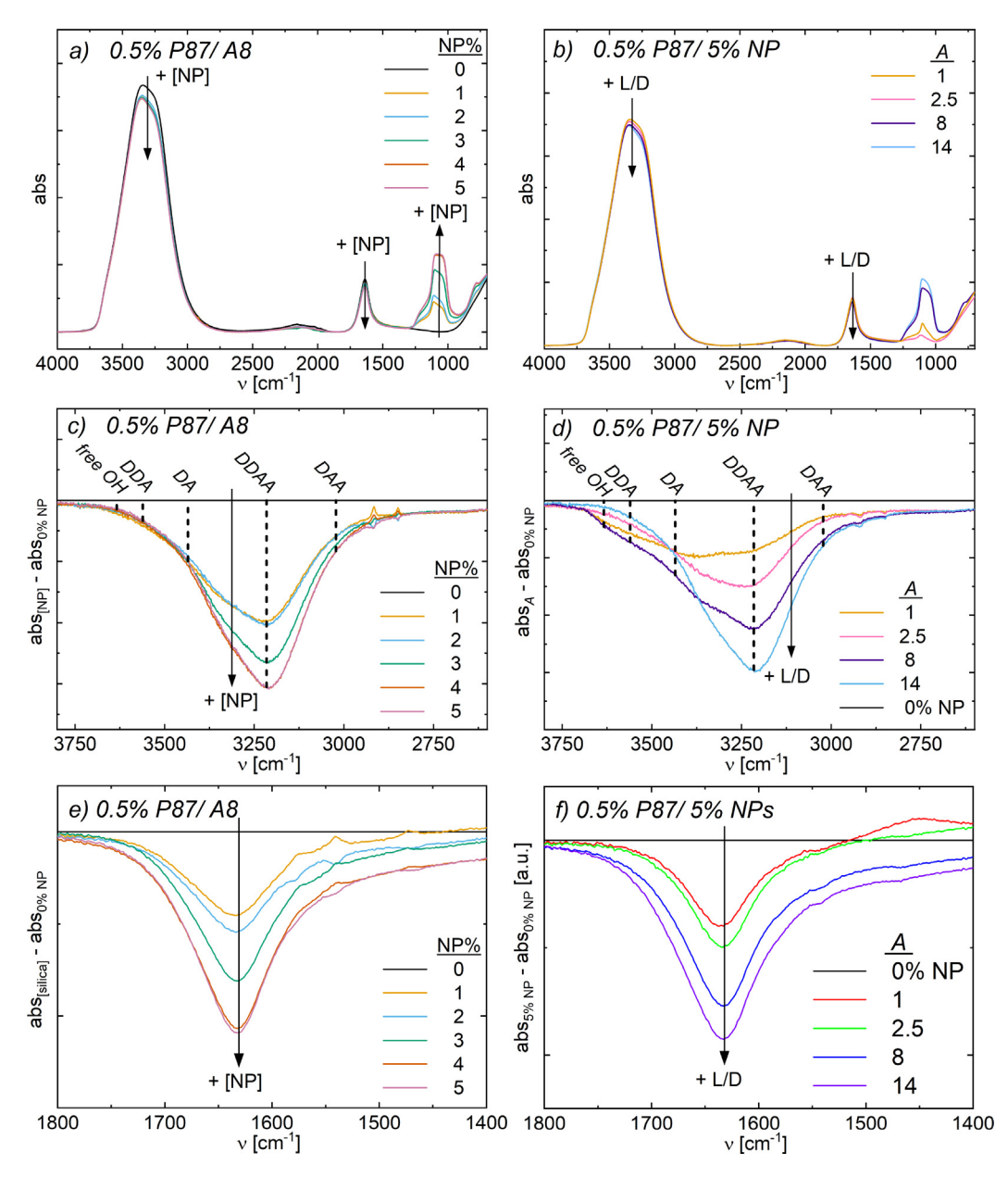


Fig. 6. FTIR spectra of 0.5% P87 across (a) A8 NP concentrations and (b) 5% NP aspect ratios. Zoomed spectra of (c,d) water-water hydrogen-bonding modes and (e,f) amidewater hydrogen-bonding modes across (c,e) A8 NP concentrations and (d,f) 5% NP aspect ratios are subtracted from 0% NP data. Peaks corresponding to H-bonding in water and between amide groups and water decrease while silica peaks increase as NP content increases. Water-water H-bonding modes are shown in vertical dashed lines: DAA (3004 cm⁻¹), DDAA (3200 cm⁻¹), DA (3440 cm⁻¹), DDA (3565 cm⁻¹), and free OH (3633 cm⁻¹).

The monotonic decrease in the $1630~\rm cm^{-1}$ peak intensity with increasing aspect ratio (Fig. 6f) initially appears in conflict with the non-monotonic change in ΔH_{sep} with aspect ratio seen prior to surface area normalization (Fig. 5). However, changes in NP ζ -potential and surface charge are known to influence FTIR signatures corresponding to interactions with NPs [103,104]; the surface charge of higher aspect ratio NPs may be felt further from the NP surface and disrupt a higher number of amide-water H-bonds. Another potential explanation for the decrease in $1630~\rm cm^{-1}$ peak intensity is due to a difference in surface hydroxyl groups across the varying NP shapes [99]. Assuming the number of NP hydroxyl groups per unit area of NP is approximately constant across NP shapes [69], as total NP surface area decreases so too should the total number of NP hydroxyl groups yielding a decrease in the NP hydroxyl group contribution to the $1630~\rm cm^{-1}$ peak.

3.3. Thermodynamic transitions at higher polymer content

To determine the impact of NP addition on PNIPAM solutions at more application-relevant concentrations [105,106], aqueous solutions with higher concentration (2% and 6%) and molecular weights ($M_n \sim 87 \text{ kDa}$ and 310 kDa) of PNIPAM were investigated with DSC. In the absence of NPs, phase separation enthalpy increases with polymer concentration from 5.9 kJ/mol_{NIPAM} in 0.5% P87 to 6.6 kJ/mol_{NIPAM} in 6% P87, potentially due to increasing PNIPAM-PNIPAM entanglements restricting rearrangement during dehydration [23]. Consistent with 0.5% solutions, systems with NPs showed statistically significant decreases in ΔH_{sep} (Figs. 3b and 5a) but no impact on $T_{on,DSC}$ or $T_{peak,DSC}$ with increasing NP content (Table 2). Across NP shapes, addition of 0.1% NP to 2% P87 decreased ΔH_{sep} by \sim 7% (Table 2) and \sim 8% in 6% P87 (Table SI.29). In both 2% and 6% P87

Table 2 Phase separation onset $(T_{on,DSC})$, peak heat flow $(T_{peak,DSC})$ temperatures and phase separation enthalpy (ΔH_{sen}) as derived from DSC for solutions of 2% P87.

NP inclusion	$T_{on,DSC}$ [${}^{\underline{o}}$ C]	$T_{peak,DSC}$ [${}^{\circ}$ C]	ΔH _{sep} [kJ/mol _{NIPAM}]
2% P87			
0%	31.66 (0.01)	33.15 (0.01)	6.19 (0.10)
0.1% A8	31.67 (0.01)	33.19 (0.01)	5.92 (0.15)
0.5% A8	31.67 (0.02)	33.19 (0.01)	5.91 (0.05)
1.0% A8	31.68 (0.01)	33.17 (0.01)	5.70 (0.13)
1.0% A1	31.59 (0.01)	33.07 (0.02)	5.67 (0.09)
1.0% A2.5	31.66 (0.01)	33.14 (0.01)	5.67 (0.16)
1.0% A14	31.68 (0.02)	33.16 (0.01)	5.78 (0.04)

solutions, the largest reduction in enthalpy is from 0% NP to 0.1% NP, with diminishing decreases in ΔH_{sep} as NP concentration further increases (Fig. 7a, 7d).

After normalizing to total NP surface area, changes in ΔH_{sep} nearly collapse onto the same curve (Fig. 7a,d and Table 2), suggesting that in higher concentration P87 solutions, depression of phase separation enthalpy is largely dominated by total NP surface area rather than differences in NP ζ-potential. This hypothesis is supported by amide-water H-bonding FTIR signatures in 2% (Fig. 7b,c) and 6% (Fig. 7e,f) P87 solutions where the reduction in peak intensity with increasing NP content or aspect ratio is largely suppressed. In solutions of 30 nm silica nanospheres (87 m²/g), Petit et al. [48] found that complete adsorption of PNIPAM occurred around 1 g/L PNIPAM per 5 g/L NP. Thus in the more concentrated P87 solutions here with much higher PNIPAM:NP ratios, a large majority of PNIPAM chains are not directly interacting with NPs, minimizing changes in FTIR peak intensities vs. in dilute P87 solutions. However, as some chains do interact with NPs in these concentration regimes, NP content decreases separation enthalpy in all presented cases.

Solutions with higher molecular weight P310 show relatively similar trends, where statistically significant decreases in separation enthalpy are observed with increasing NP content (see SI.31,

Table S16). However, no statistically significant differences in $\Delta H_{Sep}/\%$ NP are observed between P87 and P310 solutions (2% or 6%), potentially due to larger uncertainty in the P310 data due to fewer trials. In bare PNIPAM solutions (2% and 6%), the temperature corresponding with the maximum heat flow in the DSC trace, $T_{peak,DSC}$, decreases with molecular weight (33.2 °C in 2% P87 vs. 32.5 °C in 2% P310)—as expected based on worsened solubility with increasing M_n [73]. This difference in $T_{peak,DSC}$ drops to ~0.3 °C in 6% solutions. For bare PNIPAM solutions, $T_{peak,DSC}$ also exhibits a concentration-dependence, where $T_{peak,DSC}$ is >0.5 °C lower in 6% solutions (Table 2).

Across the bare and NP-containing solutions, the full-width at half maximum (FWHM) of the DSC peak for P310 solutions is 60% lower than for P87 solutions (\sim 1.0 °C vs. \sim 2.4 °C), despite the larger polydispersity of P310; this finding is also independent of temperature ramp rate (Table SI.29). An inverse relationship between phase separation width and molecular weight is expected to arise from worsening solubility of long PNIPAM chains, which leads to a more thermodynamically favorable separation that requires less energy input and proceeds at an elevated rate [74,75]. In P310 solutions, minimal differences in FWHM are observed with increasing NP (A8) or polymer content (Table SI.29).

3.4. Turbidimetric phase separation of PNIPAM-NP solutions

Comparable to findings from DSC, turbidimetry displays a single broad transition corresponding to macroscopic phase separation and PNIPAM mesoglobule formation (see SI.36 for all traces). As shown in Fig. 8 and Table 3 for 2% P87/A8 solutions, increasing NP content shifts early measures of opacity change, $T_{low,CP}$ and $T_{on,CP}$, to lower temperatures and broadens the optical phase transition. These trends are similar across NP aspect ratios; see SI.27 for values. Decreasing $T_{low,CP}$ and $T_{on,CP}$ with increasing NP content suggest that the PNIPAM chains and PNIPAM-coated NPs more readily aggregate, which can be rationalized by both PNIPAM-NP interactions and depletion attractions. For all solutions examined in this work, PNIPAM saturates the NP surface and most PNIPAM chains

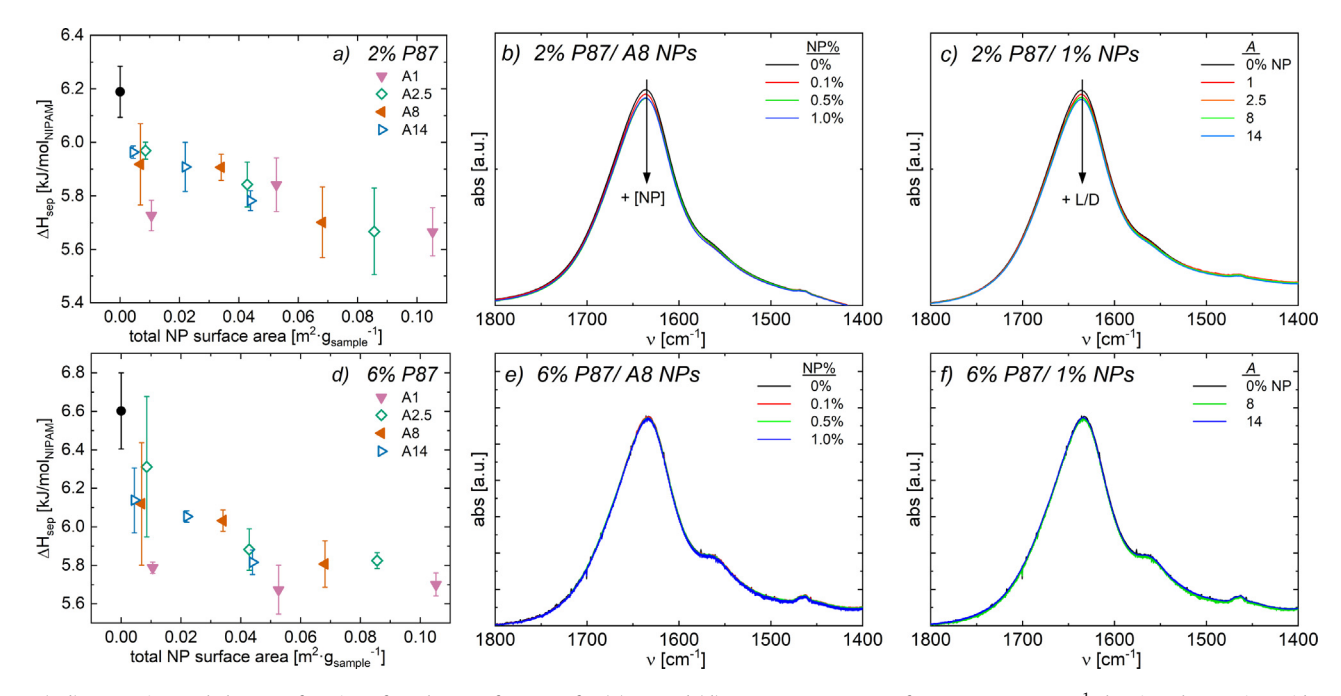


Fig. 7. (a,d) Separation enthalpy as a function of total NP surface area for (a) 2% and (d) 6% P87. FTIR spectra from 1400–1800 cm⁻¹ showing changes in amide-water hydrogen bonding for (b,c) 2% and (e,f) 6% P87. (b) and (e) show changes in amide-water hydrogen bonding as a function of A8 NP content. (c) and (f) show changes in amide-water hydrogen bonding as a function of NP aspect ratio of 1% NP solutions.

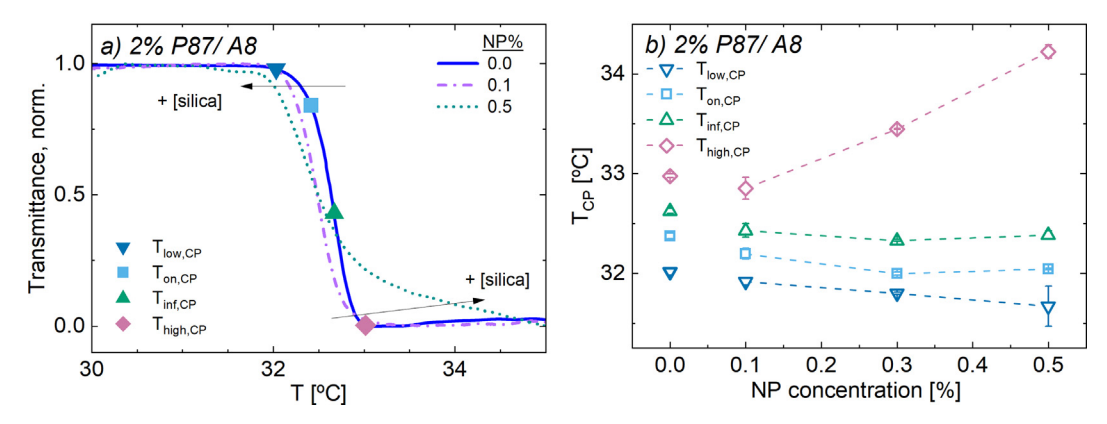


Fig. 8. (a) Transmittance vs. temperature of 2% P87/A8 NPs. As NP content increases, transition broadens and $T_{on,CP}$ decreases. Transition temperatures for bare 2% P87 are shown by symbols on the turbidimetry curve. (b) Transition temperatures of 2% P87/A8, derived from turbidimetry. Transition temperatures are also quantified in Table 3. As NP content increases, onset transition temperatures decrease whereas higher temperature measures, $T_{high,CP}$, increase.

Table 3 Transition temperatures as derived from turbidimetry $(T_{X/P})$ for solutions of 2% P87/ A8 NPs. Numbers in parentheses designate standard error $(n \ge 3)$.

NP inclusion	T _{low,CP} [°C]	<i>T_{on,CP}</i> [² C]	T _{inf,CP} [°C]	<i>T_{high,CP}</i> [ºC]
2% P87				
0%	32.06 (0.03)	32.37 (0.03)	32.62 (0.02)	33.01 (0.02)
0.1% A8	31.88 (0.04)	32.14 (0.06)	32.36 (0.07)	32.78 (0.11)
0.3% A8	31.80 (0.01)	32.02 (0.02)	32.36 (0.01)	33.48 (0.01)
0.5% A8	31.67 (0.2)	32.04 (0.08)	32.38 (0.04)	34.23 (0.07)

remain dissolved in solution, inducing a depletion attraction between NPs (see SI.11). Additionally, while the PNIPAM adsorbed to the NP surface provides steric stabilization, adsorbed polymer will also attenuate the electrostatic repulsion which stabilizes NP-only solutions (Fig. 5b), further promoting aggregation. Thus these interactions promote formation of larger polymer-NP aggregates that scatter light, thereby decreasing $T_{low,CP}$ and $T_{on,CP}$.

The decrease in $T_{on,CP}$ with NP content is -0.34 ± 0.06 °C from 0% to 0.5% NP (Table 3), suggesting that NPs promote a lower-temperature onset of clouding ($T_{on,CP}$). The 2% P310 solutions behave similarly to the P87 solutions, showing decreases in $T_{low,CP}$ and $T_{on,CP}$ with increasing NP content up to 0.5% A8 NPs (S60). The onset turbidimetric temperature of 2% P310 decreases by -0.48 ± 0.11 °C from 0% NP to 0.5% NP, statistically equal to that for 2% P87.

While the temperature corresponding to the inflection of transmittance vs. temperature, $T_{inf,CP}$, decreases upon the addition of 0.1% A8 NPs, increasing NP content further does not have any effect (Fig. 8), largely due to a transition broadening with increasing NP content. Additionally, the temperature corresponding with the end of optical transition, $T_{high,CP}$, strongly increases with NP concentration due to the observed transition broadening (Fig. 8b). This broadened transition suggests that polymers in NP-containing solutions do not fully aggregate until higher temperatures vs. PNIPAM-only solutions, which could result from the steric stabilization provided by the bound polymer layer, or that the bound polymer has reduced chain mobility which hinders subsequent collapse.

Interestingly, while $T_{low,CP}$, $T_{on,CP}$, and $T_{high,CP}$ depend on NP content, DSC separation temperatures ($T_{x,DSC}$) are statistically independent of NP content (Fig. 7, Table 2). One potential explanation for these differences is the difference in temperature ramp rate of DSC vs. turbidimetry (1.0 °C/min vs. 0.2 °C/min, respectively), which may have minimized changes in the DSC onset temperature

[16,75]. Additionally, these transition temperatures likely depend on NP content differently, as turbidimetry captures the formation of polymer-NP aggregates that can occur prior to phase separation due to reduced colloidal stability, whereas DSC captures polymer chain collapse and thermodynamic changes across the phase separation. While PNIPAM-NP H-bonds make the phase separation more thermodynamically favorable (decreasing ΔH_{sep}), extensive PNIPAM dehydration is not induced at lower temperatures ($T_{on,DSC}$). However, PNIPAM chains adsorbed onto NPs likely reduce the inter-particle electrostatic repulsion while dissolved polymers induce a depletion attraction, promoting aggregate formation and a change in opacity at a lower temperature ($T_{on,CP}$).

3.5. Temperature-dependent rheological behavior

Linear viscoelastic (LVE) rheology of P87 and P310 solutions reveals complex rheological transitions dependent on NP content and aspect ratio which are not observed in the single thermal transition from DSC or turbidimetry. In oscillatory temperature ramps of PNIPAM above a critical polymer concentration (dependent on M_n , solvent, etc.), the onset of phase separation typically corresponds to a distinct increase in dynamic moduli [48,107–109]. As the phase separation temperature is exceeded, polymer–polymer associations are more energetically favorable than polymer-water ones; PNIPAM-PNIPAM interactions then form a weakly attracting PNIPAM mesoglobule cluster network that spans the solution volume [110–113]. Consistent with this expected behavior, solutions of both P87 and P310 in the absence of nanorods exhibit a rapid increase in G_1 near 32 °C (Figs. 9, 10).

3.5.1. LVE rheology of P87/NP solutions

Adding 1% A8 NPs to 2% P87 solutions decreases the onset of the rheological transition, $T_{on,rheo}$, from 32.2 °C to 31.0 °C (Fig. 9a). As discussed in Section 3.4, both adsorbed and dissolved PNIPAM

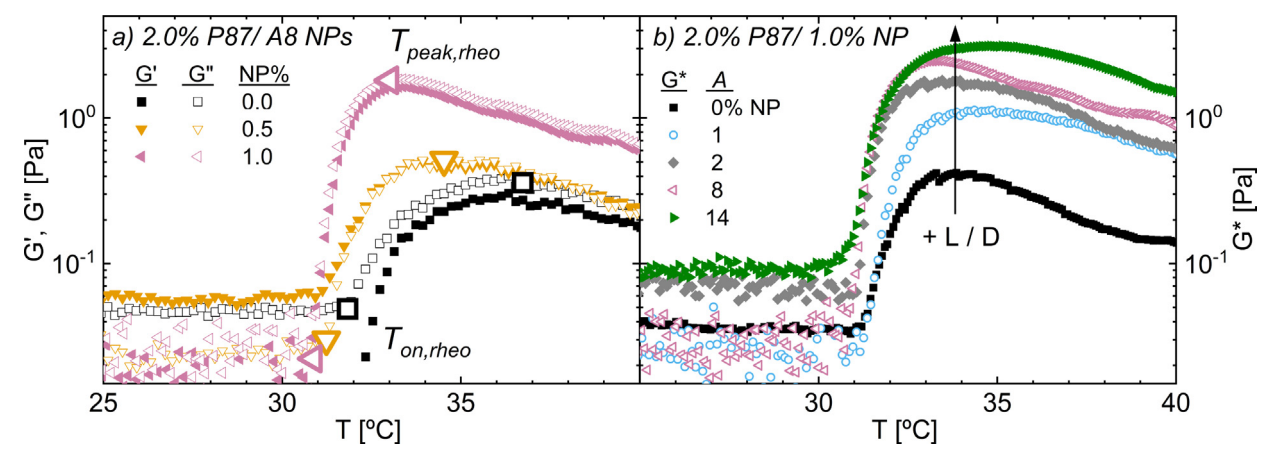


Fig. 9. Oscillatory temperature ramps of 2% P87 solutions as a function of increasing (a) A8 NP content, and (b) NP aspect ratio (1% NP). In (a), enlarged points correspond to either $T_{on,theo}$ (T < 32 °C) or $T_{peak,theo}$ (T > 32 °C). Increasing either the NP content or NP aspect ratio increases the peak modulus and maximum modulus slope.

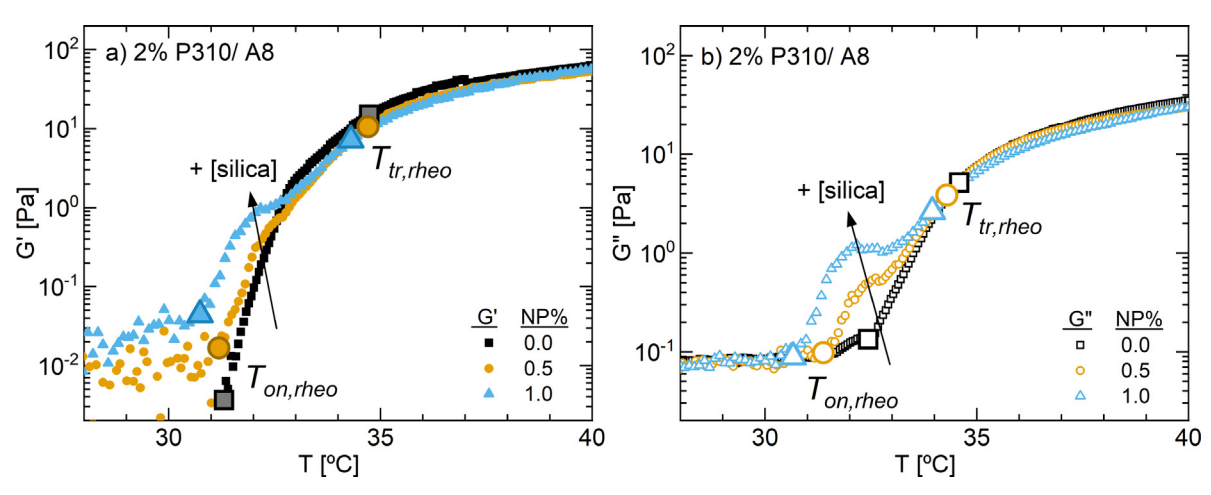


Fig. 10. Oscillatory temperature ramps of 2% P310 with A8 nanorods. Solutions transition above approx. 31 °C. (a) Storage moduli and (b) loss moduli as functions of temperature. Enlarged data points correspond to onset temperatures (*T* < 32 °C) and main rheological transition temperatures (*T* > 32 °C).

chains reduce the colloidal stability of NP-containing solutions and promote formation of PNIPAM-NP clusters which are sterically stabilized by the bound polymer layer, resulting in a rheological transition at lower temperatures. Increasing the NP content also increases the maximum slope of the dynamic moduli following the transition onset, in direct contrast to the turbidimetric transition which instead broadens with added NPs (Fig. 8a). Here, the maximum slope in G'' with temperature increases from $\sim 0.2 \text{ Pa/}^{\circ}\text{C}$ (no NPs) to 1.4 Pa/°C (1% A8 NPs, Fig. 9). Even when the moduli are normalized by peak values (see SI.33), the maximum slope of the complex modulus G^{*} still increases from 0% NP to 1% A1 NPs and further to 1% A > 1 NPs.

Across 2% P87/NP solutions, the dynamic moduli peak between 32–35 °C. With increasing NP content, the peak modulus increases, whereas the temperature at which the peak modulus is achieved, $T_{peak,rheo}$, decreases. The steeper slope and higher peak moduli with increasing NP content suggest that NPs contribute to the mechanical properties in the lower temperature ($T \sim 31-33$ °C) portion of the transition, forming a microstructure which is stronger than in the absence of NPs. With further temperature increases, the dynamic moduli decay in all solutions, likely due to polymer dehydration and collapse, which reduces the total volume fraction in solution as potential inter-aggregate linkages are broken and the adsorbed layer thickness on the NP is reduced (see SI.10). Any potential steric stabilization provided by the adsorbed PNIPAM

brush is also likely mitigated as the layer thickness shrinks and solvent quality worsens at higher temperatures. Above 35 °C, the rate of decay in complex modulus (G^*) with temperature appears independent of NP concentration (Fig. 9a), supporting the idea that the weakened microstructure at high temperatures is largely due to polymer chain collapse. This lower molecular weight solution is near the overlap concentration at ambient conditions (SI.17), enabling an increase in modulus as polymer-NP aggregates form; however, a reduction in the polymer pervaded volume with increasing temperature and a lack of extensive entanglements (see SI.14) could prevent a system-spanning network from forming at elevated temperatures.

In contrast to increasing NP content, increasing the NP aspect ratio in 0.5% (Fig. S53) and 1% NP solutions does not measurably change the rheological transition onset or the rate at which G^* increases following $T_{on,rheo}$ (Fig. 9b). However, the peak modulus does increase with NP aspect ratio. Higher aspect ratio NPs contain more silanol binding sites per NP than low A NPs, allowing longer NPs to act as inorganic cross linkages between PNIPAM clusters. Longer nanorods also have a lower minimum interparticle distance (SI.8), allowing for formation of more polymer bridges between particles [60]. Thus, longer nanorods likely increase the total system interconnectedness, strengthening the dynamic moduli similar to previously-reported systems of nanorod-containing hydrogel scaffolds [56,114,115]. While spherical NPs increase the

maximum complex modulus, the rate of G^* increase is below that of the A2.5 NPs, potentially due to overall NP size or differences in ζ -potential. Spherical NPs can still increase the system interconnectedness, but cannot span between PNIPAM clusters as effectively as rods. The nanospheres also have lower ζ -potential than nanorods in this work (Fig. 5b), potentially leading to weaker binding between mesoglobules vs. in higher ζ -potential nanorods. Versus 0% NP solutions, spherical NP addition may also increase G^* by increasing the effective volume fraction in these solutions, though this effect is likely small due to the low NP content.

3.5.2. LVE rheology of P310/NP solutions

The addition of NPs to P310 solutions leads to distinct rheological behavior vs. the P87/NP solutions, including the emergence of a two-step transition not previously observed. For example, when A8 NPs are added to 2% P310 solutions, a shoulder forms in the dynamic moduli near 32 °C following the transition onset Ton, rheo (Fig. 10); this shoulder stage is short-lived, persisting for only a few degrees (\sim 31–32.5 °C) (see SI.34 for more data). The onset of the rheological transition and appearance of the shoulder region shifts to lower temperatures with increasing A8 NP content (Fig. 10a, SI.16). As such, the temperature window in which this shoulder arises widens with increasing NP concentration but is relatively unaffected by NP aspect ratio (Fig. S59). The presence of a lower-temperature shoulder in dynamic moduli suggests the formation of an intermediate microstructure caused by NP aggregation and bridging between PNIPAM clusters as, at this point in the separation, PNIPAM mesoglobule clusters have minimal inter-globule interactions [22,24].

Unlike in P87 solutions, the maximum slope of Gr in 2% P310 solutions does not increase with NP content (SI.16) at the primary rheological transition ($T_{tr,rheo}$). However, the maximum slope in log Gr-corresponding to the maximum slope of the moduli shoulderdoes increase with NP content, further suggesting that NP content dictates the rheological transition in this region. The shoulder in the moduli also occurs before the transition onset temperature in either turbidimetry or DSC, suggesting that polymer chains remain primarily in the hydrated state at these temperatures and do not aggregate substantially [22]. Thus polymer–polymer associations below 32 °C are likely insufficient to form an interconnected network [22,116–118]. However polymer-NP interactions and depletion attractions may lead to formation of small clusters of increased modulus.

In P310/A8 solutions, G1 and G11 nearly perfectly coincide with those of the bare P310 solutions above 33 °C, following the shoulder in the dynamic moduli (Fig. 10). Unlike in P87 solutions in which the dynamic moduli decay at elevated temperatures, the dynamic moduli of 2% P310 increase following the shoulder region, suggesting formation of an interconnected network rather than localized polymer/NP aggregates [22,116–118]. These conclusions are unsurprising given the relative polymer sizes: R_h is twice as large for P310 as for P87, giving an estimated overlap concentration, c^* [119], that is 2.5-fold smaller for P310 ($c^* \sim 1\%$) vs. P87 ($c^* \sim 2.5\%$); see SI.17 for calculations of the overlap and entanglement concentrations. P310 is also more disperse, with a weightaverage molecular weight that is nearly eightfold larger than that of P87. Thus at ambient conditions, 2% P310 is well above c^* and the longer chains likely entangle (SI.17); conversely, after accounting for chain polydispersity, 2% P87 is likely near c* at ambient conditions but likely drops below c^* as its pervaded volume decreases with water expulsion at elevated temperatures. As such, the larger P310 chains more easily interact in solution and can form a system-spanning network, rather than localized aggregates, during phase separation. While $T_{on,rheo}$ decreases with increasing NP content, the primary temperature at which this rheological transition

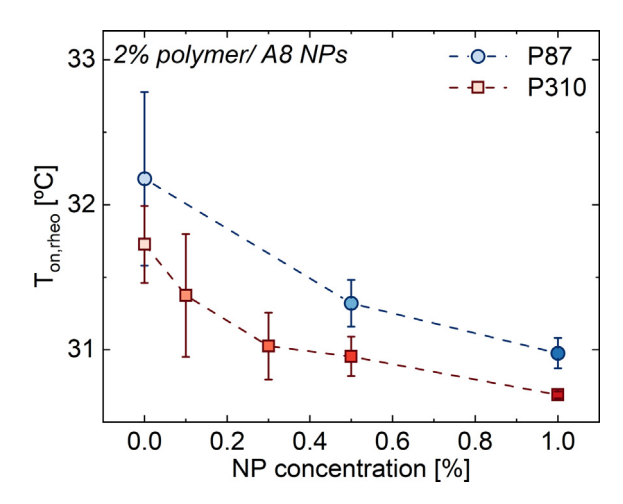


Fig. 11. Rheological transition onset temperatures for 2% P310 or P87 with A8 NPs. Increasing NP content decreases $T_{on,theo}$ by a similar degree in both P87 and P310, up to \sim 1 °C at 1% NPs. Error bars are mean standard errors ($N \geq 3$).

occurs, $T_{tr,rheo}$ (see Section 2.10), does not significantly decrease from bare to 1% NPs. Thus, the rheology of 2% P310 solutions near $T_{tr,rheo}$ is predominantly polymer dominated, and PNIPAM-NP interactions do not contribute significantly to the solution rheological response at higher temperatures.

3.5.3. Impact of PNIPAM molecular weight and NP length on phase transition

NP addition decreases the onset of the rheological transition, $T_{on,rheo}$, in both 2% P87 and P310 solutions by a similar degree (Fig. 11, Table 4). For example, adding 1% A8 NPs decreases $T_{on,rheo}$ by \sim 1 °C for both 2% PNIPAM solutions; these trends are relatively consistent across NP aspect ratios (Figs. 11, SI.34).

In both P310 and P87, the decrease in $T_{on,rheo}$ follows a similar trend with increasing NP content and appears to eventually plateau at higher NP contents (Fig. 11). The similar impact of NP addition regardless of PNIPAM molecular weight and dispersity suggests that the rheological transition onset is governed primarily by NPs rather than PNIPAM. Interestingly, the average difference between $T_{tr,rheo}$ and $T_{on,rheo}$ for P310 is nearly an order of magnitude higher than in P87 (3.1 °C vs. 0.4 °C). However notably, $T_{tr,rheo}$ corresponds to the single transition in P87 solutions vs. the transition that occurs after the shoulder region in P310 solutions, suggesting that the transition in P87 solutions is analogous to the initial, shoulder-region transition in P310 solutions.

Table 4 Rheological transition temperatures, including transition onset $(T_{on,rheo})$ and primary transition temperature $(T_{tr.theo})$ for 2% P87 and 2% P310 solutions. See Sl.28 for all rheological transition temperatures of all samples studied in this work.

NP inclusion	T _{on,rheo}	T _{tr,rheo}	dG# dT max
	[°C]	[° C]	[Pa/ºC]
2% P87			
0%	32.18 (0.60)	32.62 (0.52)	0.21 (0.04)
0.5% A8	31.32 (0.16)	31.68 (0.03)	0.30 (0.01)
1.0% A8	30.98 (0.10)	31.21 (0.05)	1.37 (0.05)
1.0% A1	31.09	32.3	0.73
1.0% A2.5	31.12 (0.11)	31.49 (0.21)	1.10 (0.20)
1.0% A14	31.03 (0.19)	31.44 (0.15)	0.87 (0.19)
2% P310			
0%	31.72 (0.27)	34.67 (0.09)	3.51 (0.82)
0.5% A8	30.95 (0.14)	33.75 (0.40)	3.53 (1.13)
1.0% A8	30.69 (0.02)	34.13 (0.02)	2.87 (0.82)
1.0% A1	30.86 (0.09)	33.96 (0.11)	6.16 (0.63)
1.0% A14	30.74 (0.04)	33.69 (0.63)	5.16 (1.05)

Comparing the dynamic moduli between 2% P87 and P310 solutions with no NPs in Fig. 12a suggests that the onset of modulus increase for bare PNIPAM solutions, $T_{on,rheo}$, occurs concurrently with the peak in DSC heat flow, $T_{peak,DSC}$. As such, the primary rheological transition in bare PNIPAM solutions is due to the dehydration of PNIPAM chains and the subsequent mesoglobule formation and growth. With 1% A8 NPs (Fig. 12b), lower-temperature modulus increase occurs before $T_{peak,DSC}$, suggesting that the first rheological transition-or the modulus increase before primary PNIPAM chain dehydration-depends primarily on PNIPAM-NP interactions that reduce the inter-particle electrostatic repulsion and inter-particle depletion attractions due to free PNIPAM, which destabilize the suspension and lead to flocculation prior to polymer dehydration and aggregation [60,83]. Further, as the loss moduli for 2% P87 and P310 with 1% A8 NPs coincide between Tonsheo and T_{peak.DSC} (30-32 °C), this lower-temperature rheological transition likely depends more on NP concentration than either polymer molecular weight or dispersity. Near $T \sim 32$ °C, the heat flow of 1% A8 NP solutions begin to rise as the moduli increase slows (Fig. 12b). At $T_{peak,DSC}$ (enlarged points), P310 moduli lag and then steadily increase until above 40 °C. P87 moduli, however, peak and decay. PNIPAM entanglements formed at low temperature become more important in the late-intermediate temperatures ($T \sim 33-34$ °C) and likely dictate whether moduli decay or grow at higher temperatures [22,116–118]. Thus the difference in rheology curves in Fig. 12 suggests that low temperature transition is dictated by colloidal stability whereas high temperature transition is determined by PNIPAM-PNIPAM interactions, with the specific trend in G^* dictated by the proximity of the solution to C^* .

Based on the culmination of rheological and thermodynamic data, two pathways for microstructure formation between PNIPAM and NPs are proposed (Fig. 13). In contrast to hydrophobically-

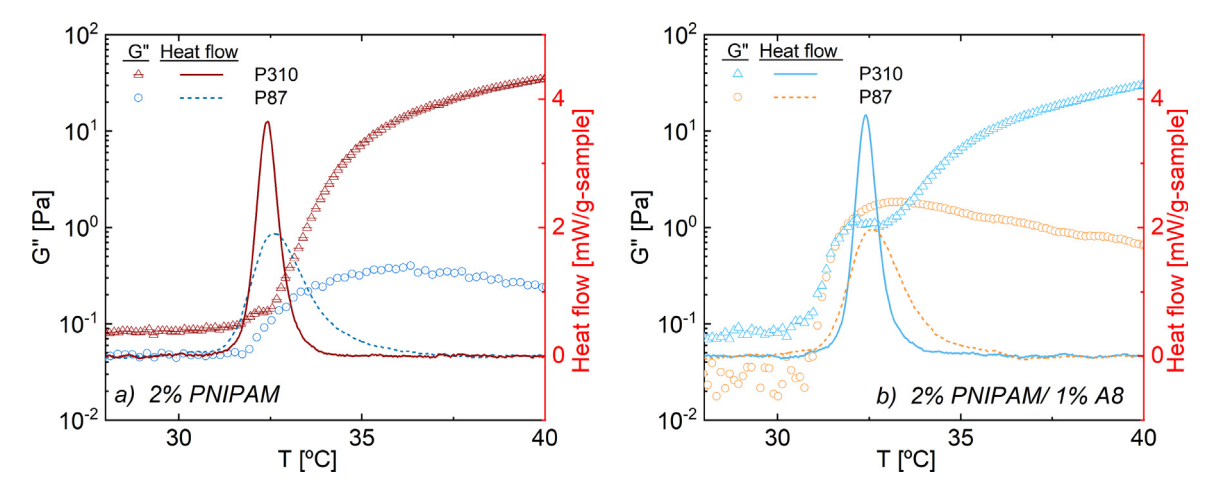


Fig. 12. Loss modulus (symbols) and cumulative ΔH_{sep} (lines) for 2% P310 (teal) and P87 (orange) with (a) no NPs and (b) 1% A8 NPs. High M_n solutions are polymer-dominated, with increasing moduli. For clarity, every 3rd point is shown. Overlaid DSC traces suggest that the shoulder from rheology corresponds to the peak in DSC heat flow

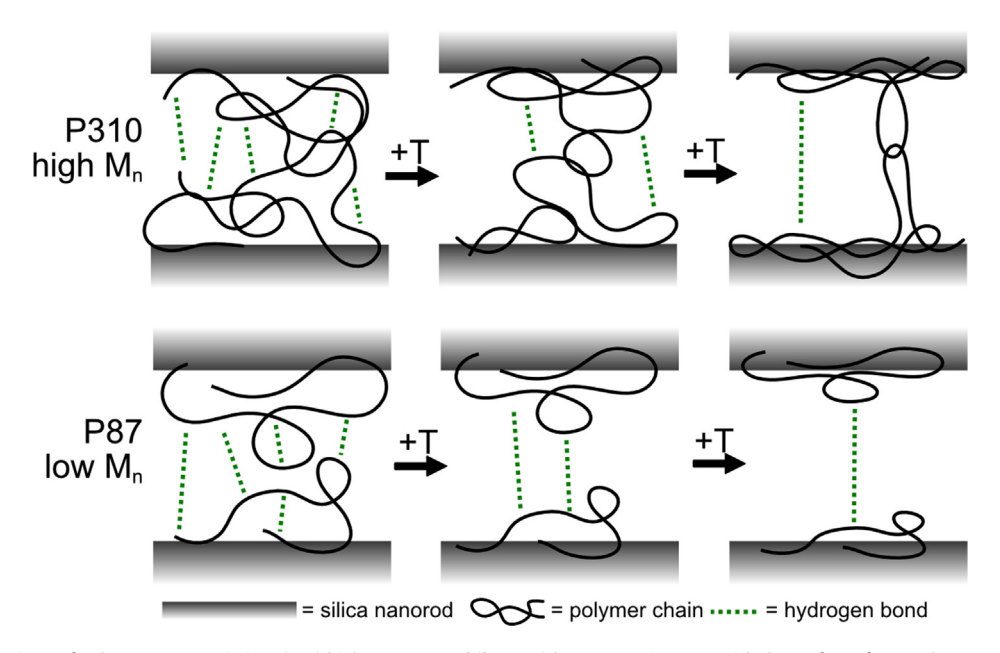


Fig. 13. Proposed mechanisms of polymer-NP association: (top) high M_n P310 and (bottom) low M_n P87 interact with the surface of NPs at low temperature, with hydrogen bonds potentially forming between chains on different NPs. As temperature increases, chains dehydrate and form mesoglobules. With high M_n P310, entanglements can form between chains on different NPs and mesoglobules coarsen to form system-spanning aggregates. In low M_n P87, however, mesoglobules do not form system-spanning aggregates at elevated temperatures. Polymers and NPs are not drawn to scale. Polymer chain symbols can signify single chains, multiple chains or mesoglobules. Due to relative sizes of NPs and polymer, NP curvature is not shown.

interacting gold NPs [64], associations with silica NPs are largely due to amide-silanol hydrogen bonding. Given the relatively high M_n and Φ of P310 (SI.17), single PNIPAM chains may associate with multiple NPs or entangle with chains on other NPs and form PNI-PAM bridges between NPs, increasing the dynamic moduli continuously at elevated temperatures (Fig. 10). In P87, however, PNIPAM adsorbed onto the NP surface likely does not entangle with chains adsorbed on other NPs. In either case, as temperature increases further, PNIPAM-PNIPAM interactions become more thermodynamically favorable, leading to chain collapse and mesoglobule formation. In high M_n PNIPAM solutions with concentrations well above c^* , mesoglobules remain interconnected and strengthen the gel. In P87, however, chain collapse likely leads to smaller mesoglobules that do not span the solution, causing the modulus decay. Thus while NPs can impact the PNIPAM separation route, the ability for NP shape to impact PNIPAM rheology also depends largely on polymer properties and a balance of PNIPAM-PNIPAM and PNIPAM-NP interactions.

Finally, while the complex modulus increases at a similar rate across NP aspect ratios in 2% P87 solutions (Fig. 9b), peak modulus values, G_{peak}^* , are correlated with aspect ratio, again suggesting that longer NPs span more of the solution and associate with a larger number of PNIPAM chains per rod, creating a stronger microstructure. This positive trend in complex modulus with aspect ratio appears to remain even at higher temperatures (T > 35 °C) after thorough polymer dehydration. As such, tailoring silica NP aspect ratio is yet another method to control the strength of thermoresponsive mesoglobules, although polymer concentration and M_n must also be considered. Given extensive research on altering the size and shape of silica NPs [67,120–122], use of distinct NP shapes including platelets and complex prisms may yield additional routes for controlling these properties.

4. Conclusion

Both the quantity and shape of anisotropic silica nanoparticles (NPs) added to aqueous poly(N-isopropyl acrylamide) (PNIPAM) solutions alter the temperature-dependent phase separation and rheological properties. NPs at concentrations as low as 0.1% promote hydrogen bonding interactions between the NP surface silanol groups and polymer amide group, which replace hydrogen bonds with water and reduce the intensity of the amide-water H-bonding peak in FTIR spectra. For all polymer concentrations investigated in this work, increasing NP content decreases the enthalpy of phase separation, ΔH_{sep} , as these polymer-NP associations reduce the number of polymer-water H-bonds to be broken during phase separation. In low PNIPAM content solutions (0.5%), higher NP aspect ratios decrease ΔH_{sep} more substantially per equivalent surface area. This finding is likely due to the increasing NP ζ-potential and surface silanol density with increasing NP aspect ratio, in contrast to prior work on PNIPAM/hydrophobic gold nanorod solutions that suggested that changes in phase separation temperatures resulted from changes in NP aspect ratio and curvature [64]. In higher PNIPAM concentration solutions (2% and 6%) with equivalent NP content, no statistically significant differences in ΔH_{sep} are observed based on aspect ratio. In these more concentrated solutions, the intensity of the amide-water Hbonding peak in the FTIR spectra is reduced only minimally due to NP inclusion, suggesting that a smaller fraction of PNIPAM chains interact with NPs and thus PNIPAM-PNIPAM interactions and entanglements instead dominate the phase separation behavior.

While thermodynamic and optical measurements suggest relatively minor changes in phase separation behavior with NP addition, oscillatory rheology suggests that NP inclusion alters the

pathway for chain collapse and agglomeration. Differential scanning calorimetry and rheological temperature ramps on aqueous PNIPAM confirm that with increasing temperature, PNIPAM chains first collapse then agglomerate into clusters or flocks that attract each other. However with NP addition, depending on polymer molecular weight, a peak (87 kDa) or shoulder (310 kDa) in the dynamic moduli appears with increasing temperature far prior to the thermal transition observed in the bare solutions. The onset of this transition decreases with increasing NP content, suggesting that overlapping PNIPAM-NP clusters form prior to extensive PNI-PAM chain collapse, increasing the modulus. Interestingly, in 87 kDa PNIPAM solutions, higher aspect ratio NPs result in higher maximum complex moduli during this stage, suggesting that the mechanical properties can be tuned via both NP content and NP aspect ratio: future investigations using distinct NP shapes could provide additional routes for finely controlling the properties of these thermoresponsive systems. With further temperature elevation, PNIPAM chains either entangle and form strong hydrogels (310 kDa) or weakly interact through attractive forces (87 kDa). These results demonstrate that the thermodynamic, optical and rheological properties of aqueous PNIPAM solutions can be finely tuned via the concentration and shape of hydrophilicallyinteracting silica NPs, allowing for more robust applications for thermally-responsive systems.

Declaration of Competing Interest

The authors declare that they have no known competing financial interests or personal relationships that could have appeared to influence the work reported in this paper.

Acknowledgements

Research reported in this publication was supported by the Office of the Vice President of Research, College of Science and Engineering, and the Department of Chemistry at the University of Minnesota. Research reported in this publication was supported by the Office of the Director, National Institutes of Health, [Award Number S100D011952]; the content is solely the responsibility of the authors and does not necessarily represent the official views of the National Institutes of Health. The authors thank the Anton Paar VIP program for the rheometer used in this work. Research reported in this publication was supported by the Office of the Vice President of Research, College of Science and Engineering, and the Department of Chemistry at the University of Minnesota. This work was supported partially by the Partnership for Research and Education in Materials (PREM) Program of the National Science Foundation under Award Number DMR-2122178, and through the University of Minnesota MRSEC under Award Number DMR-2011401. The authors would like to thank Benjamin Yeh of the Bhan research group at the University of Minnesota-Twin Cities for running BET measurements and analysis. Solid state NMR data was provided by the Minnesota NMR Center. Funding for NMR instrumentation was provided by the Office of the Vice President for Research, the Medical School, the College of Biological Science. NIH, NSF, and the Minnesota Medical Foundation.

Appendix A. Supplementary material

Supplementary data to this article can be found online at https://doi.org/10.1016/j.jcis.2022.08.139.

References

 P. Peumans, S.R. Forrest, Very-high-efficiency double-heterostructure copper phthalocyanine/C60 photovoltaic cells, Appl. Phys. Lett. 79 (1) (2001) 126– 128, https://doi.org/10.1063/1.1384001.

- [2] D.-H. Kim, J. Xiao, J. Song, Y. Huang, J.A. Rogers, Stretchable, Curvilinear Electronics Based on Inorganic Materials, Adv. Mater. 22 (19) (2010) 2108– 2124, https://doi.org/10.1002/adma.200902927.
- [3] Q. Cao, J.A. Rogers, Ultrathin Films of Single-Walled Carbon Nanotubes for Electronics and Sensors: A Review of Fundamental and Applied Aspects, Adv. Mater. 21 (1) (2009) 29–53, https://doi.org/10.1002/adma.200801995.
- [4] I. Tokarev, S. Minko, Multiresponsive, hierarchically structured membranes: new, challenging, biomimetic materials for biosensors, controlled release, biochemical gates, and nanoreactors, Adv. Mater. 21 (2) (2009) 241–247, https://doi.org/10.1002/adma.200801408.
- [5] K. Vaeth, OLED-Display Technology-OLEDs are exciting not only because of their excellent front-of-screen performance, but because their flexibility invites many approaches to materials and device design., in: Information display., Vol. 19, 2003, p. 12.
- [6] S.R. Forrest, The path to ubiquitous and low-cost organic electronic appliances on plastic, Nature 428 (6986) (2004) 911–918, https://doi.org/ 10.1038/nature02498.
- [7] S.E. Shaheen, C.J. Brabec, N.S. Sariciftci, F. Padinger, T. Fromherz, J.C. Hummelen, 2.5% efficient organic plastic solar cells, Appl. Phys. Lett. (2001) 841–843, https://doi.org/10.1063/1.1345834.
- [8] M. Granström, K. Petritsch, A.C. Arias, A. Lux, M.R. Andersson, R.H. Friend, Laminated fabrication of polymeric photovoltaic diodes, Nature 395 (6699) (1998) 257–260, https://doi.org/10.1038/26183.
- [9] P. Peumans, S. Uchida, S.R. Forrest, Efficient bulk heterojunction photovoltaic cells using small-molecular-weight organic thin films, in: Mater. Sustainable Energy, Co-Published with Macmillan Publishers Ltd, UK, 2010, pp. 94–98.
- [10] L. He, Y. Hu, H. Kim, J. Ge, S. Kwon, Y. Yin, Magnetic Assembly of Nonmagnetic Particles into Photonic Crystal Structures, Nano Lett. 10 (11) (2010) 4708– 4714, https://doi.org/10.1021/nl103008v.
- [11] S.A. Asher, J. Holtz, L. Liu, Z. Wu, Self-Assembly Motif for Creating Submicron Periodic Materials. Polymerized Crystalline Colloidal Arrays, J. Am. Chem. Soc. 116 (11) (1994) 4997–4998, https://doi.org/10.1021/ja00090a059.
- [12] G. Pan, R. Kesavamoorthy, S.A. Asher, Nanosecond Switchable Polymerized Crystalline Colloidal Array Bragg Diffracting Materials, J. Am. Chem. Soc. 120 (26) (1998) 6525–6530, https://doi.org/10.1021/ja980481a.
- [13] E. Choi, J. Brooks, D. Eaton, M. Al-Haik, M. Hussaini, H. Garmestani, D. Li, K. Dahmen, Enhancement of thermal and electrical properties of carbon nanotube polymer composites by magnetic field processing, J. Appl. Phys. 94 (9) (2003) 6034–6039, https://doi.org/10.1063/1.1616638.
- [14] T. Kimura, H. Ago, M. Tobita, S. Ohshima, M. Kyotani, M. Yumura, Polymer composites of carbon nanotubes aligned by a magnetic field, Adv. Mater. 14 (19) (2002) 1380–1383, https://doi.org/10.1002/1521-4095(20021002) 14:19<1380::AID-ADMA1380>3.0.CO;2-V.
- [15] R. Andrews, D. Jacques, A. Rao, T. Rantell, F. Derbyshire, Y. Chen, J. Chen, R. Haddon, Nanotube composite carbon fibers, Appl. Phys. Lett. 75 (9) (1999) 1329–1331, https://doi.org/10.1063/1.124683.
- [16] Z. Osváth, B. Iván, The Dependence of the Cloud Point, Clearing Point, and Hysteresis of Poly(N-isopropylacrylamide) on Experimental Conditions: The Need for Standardization of Thermoresponsive Transition Determinations, Macromol. Chem. Phys. 218 (4) (2017) 1600470, https://doi.org/ 10.1002/macp.201600470.
- [17] J.C. Garbern, A.S. Hoffman, P.S. Stayton, Injectable pH- and Temperature-Responsive Poly(N-isopropylacrylamide-co-propylacrylic acid) Copolymers for Delivery of Angiogenic Growth Factors, Biomacromolecules 11 (7) (2010) 1833–1839, https://doi.org/10.1021/bm100318z.
- [18] B. Jeong, Y.H. Bae, D.S. Lee, S.W. Kim, Biodegradable block copolymers as injectable drug-delivery systems, Nature 388 (6645) (1997) 860–862, https://doi.org/10.1038/42218.
- [19] L.E. Bromberg, E.S. Ron, Temperature-responsive gels and thermogelling polymer matrices for protein and peptide delivery, Adv. Drug Deliv. Rev. 31 (3) (1998) 197–221. https://doi.org/10.1016/S0169-409X(97)00121-X.
- [20] A. Serres, M. Baudyš, S.W. Kim, Temperature and pH-sensitive Polymers for Human Calcitonin Delivery, Pharm. Res. 13 (2) (1996) 196–201, https://doi. org/10.1023/A:1016026711364.
- [21] K. Shiraga, H. Naito, T. Suzuki, N. Kondo, Y. Ogawa, Hydration and Hydrogen Bond Network of Water during the Coil-to-Globule Transition in Poly(Nisopropylacrylamide) Aqueous Solution at Cloud Point Temperature, J. Phys. Chem. B 119 (17) (2015) 5576–5587, https://doi.org/10.1021/acs. ipcb_5b01021
- [22] I. Bischofberger, V. Trappe, New aspects in the phase behaviour of poly-N-isopropyl acrylamide: systematic temperature dependent shrinking of PNiPAM assemblies well beyond the LCST, Scientific Reports 5 (1) (2015) 15520, https://doi.org/10.1038/srep15520.
- [23] L. Song, J. Lin, P. Liu, J. Li, S. Jiang, D. Huang, Quantitative determination of the spring entropy effect and its indication of the conformational change of polymer coils with varying concentration in aqueous poly(N-isopropylamide) solutions, RSC Advances 9 (10) (2019) 5540–5549, https://doi.org/10.1039/ C9RA00117D.
- [24] A. Halperin, M. Kröger, F.M. Winnik, Poly(N-isopropylacrylamide) Phase Diagrams: Fifty Years of Research, Angew. Chem. Int. Ed. 54 (51) (2015) 15342–15367, https://doi.org/10.1002/anie.201506663.
- [25] A.V. Gorelov, A. Du Chesne, K.A. Dawson, Phase separation in dilute solutions of poly (N-isopropylacrylamide), Physica A 240 (3) (1997) 443–452, https:// doi.org/10.1016/S0378-4371(97)00192-1.
- [26] P. Kujawa, V. Aseyev, H. Tenhu, F.M. Winnik, Temperature-Sensitive Properties of Poly(N-isopropylacrylamide) Mesoglobules Formed in Dilute

- Aqueous Solutions Heated above Their Demixing Point, Macromolecules 39 (22) (2006) 7686–7693, https://doi.org/10.1021/ma061604b.
- [27] C. Wu, W. Li, X.X. Zhu, Viscoelastic Effect on the Formation of Mesoglobular Phase in Dilute Solutions, Macromolecules 37 (13) (2004) 4989–4992, https://doi.org/10.1021/ma049556n.
- [28] G. Zhang, C. Wu, Folding and Formation of Mesoglobules in Dilute Copolymer Solutions, in: A.R. Khokhlov (Ed.), Conformation-Dependent Design of Sequences in Copolymers I, Springer, Berlin, Heidelberg, 2006, pp. 101–176, https://doi.org/10.1007/12_050.
- [29] K.A. Dawson, A.V. Gorelov, E.G. Timoshenko, Y.A. Kuznetsov, A. Du Chesne, Formation of mesoglobules from phase separation in dilute polymer solutions: a study in experiment, theory, and applications, Physica A 244 (1) (1997) 68–80, https://doi.org/10.1016/S0378-4371(97)00299-9.
- [30] L. Botto, E.P. Lewandowski, M. Cavallaro, K.J. Stebe, Capillary interactions between anisotropic particles, Soft Matter 8 (39) (2012) 9957–9971, https://doi.org/10.1039/c2sm25929j.
- [31] R. Krishnamoorti, R.A. Vaia, Polymer nanocomposites, J. Polym. Sci., Part B: Polym. Phys. 45 (24) (2007) 3252–3256, https://doi.org/10.1002/polb.21319.
- [32] P. Akcora, H. Liu, S.K. Kumar, J. Moll, Y. Li, B.C. Benicewicz, L.S. Schadler, D. Acehan, A.Z. Panagiotopoulos, V. Pryamitsyn, V. Ganesan, J. Ilavsky, P. Thiyagarajan, R.H. Colby, J.F. Douglas, Anisotropic self-assembly of spherical polymer-grafted nanoparticles, Nat. Mater. 8 (4) (2009) 354–359, https://doi.org/10.1038/NMAT2404.
- [33] Z. Zhai, Q. Wu, J. Li, B. Zhou, J. Shen, Z.H. Farooqi, W. Wu, Enhanced catalysis of gold nanoparticles in microgels upon on site altering the gold-polymer interface interaction, J. Catal. 369 (2019) 462–468, https://doi.org/10.1016/j. jcat.2018.10.037.
- [34] S.A. Jadhav, V. Brunella, I. Miletto, G. Berlier, D. Scalarone, Synthesis of poly(n-isopropylacrylamide) by distillation precipitation polymerization and quantitative grafting on mesoporous silica, J. Appl. Poly. Sci. 133 (44) (2016), https://doi.org/10.1002/app.44181.
- [35] S.A. Jadhav, V. Brunella, S. Sapino, B. Caprarelli, C. Riedo, D. Chirio, M. Gallarate, Poly (n-isopropylacrylamide) based hydrogels as novel precipitation and stabilization media for solid lipid nanoparticles (SLNs), J. Colloid Interface Sci. 541 (2019) 454–460. doi:10.1016/j.jcis.2019.01.107.
- [36] J. Kopecek, Smart and genetically engineered biomaterials and drug delivery systems, Eur. J. Pharm. Sci. 20 (1) (2003) 1–16, https://doi.org/10.1016/ S0928-0987(03)00164-7.
- [37] C. d. l. H. Alarcón, S. Pennadam, C. Alexander, Stimuli responsive polymers for biomedical applications, Chem. Soc. Rev. 34 (3) (2005) 276–285, https://doi. org/10.1039/B406727D.
- [38] R. Yerushalmi, A. Scherz, M.E. v. d. Boom, H.-B. Kraatz, Stimuli responsive materials: new avenues toward smart organic devices, J. Mater. Chem. 15 (42) (2005) 4480-4487, https://doi.org/10.1039/B505212B.
- [39] Y. Qiu, K. Park, Environment-sensitive hydrogels for drug delivery, Adv. Drug Deliv. Rev. 53 (3) (2001) 321–339, https://doi.org/10.1016/S0169-409X(01) 00203-4
- [40] M.A. Uddin, H. Yu, L. Wang, J. Liu, S. Mehmood, B.U. Amin, F. Haq, R. Liang, D. Shen, Z. Ni, Multi-stimuli-responsive performance and morphological changes of radical-functionalized self-assembled micellar nanoaggregates and their multi-triggered drug release, Colloids Surf. A Physicochem. Eng. Asp. 625 (2021) 126807, https://doi.org/10.1016/j.colsurfa.2021.126807.
- [41] S.A. Jadhav, R. Nisticó, G. Magnacca, D. Scalarone, Packed hybrid silica nanoparticles as sorbents with thermo-switchable surface chemistry and pore size for fast extraction of environmental pollutants, RSC Adv 8 (3) (2018) 1246–1254, https://doi.org/10.1039/C7RA11869D.
- [42] M.E. Peralta, S.A. Jadhav, G. Magnacca, D. Scalarone, D.O. Mártire, M.E. Parolo, L. Carlos, Synthesis and in vitro testing of thermoresponsive polymer-grafted core-shell magnetic mesoporous silica nanoparticles for efficient controlled and targeted drug delivery, J. Colloid Interface Sci. 544 (2019) 198–205, https://doi.org/10.1016/j.jcis.2019.02.086.
- [43] S.A. Jadhav, V. Spalletta, D. Scalarone, Thermally triggered on demand permeability of hybrid silica beds made of packed thermoresponsive organo-silica microparticles, eXPRESS Poly, Lett 13 (1) (2019) 84–95, https://doi.org/10.3144/expresspolymlett.2019.8.
- (44) S.A. Jadhav, D. Scalarone, V. Brunella, E. Ugazio, S. Sapino, G. Berlier, Thermoresponsive copolymer-grafted SBA-15 porous silica particles for temperature-triggered topical delivery systems, eXPRESS Poly, Lett 11 (2) (2017) 96–105, https://doi.org/10.3144/expresspolymlett.2017.11.
 [45] M. Tanahashi, K. Takeda, Dispersion of Nano-Sized Hydrophilic Silica Particles
- [45] M. Tanahashi, K. Takeda, Dispersion of Nano-Sized Hydrophilic Silica Particles into Various Hydrophobic Polymer Networks, J. of Nanosci. Nanotechnol. 14 (4) (2014) 3123–3136, https://doi.org/10.1166/jnn.2014.8601.
- [46] J. Parvole, L. Ahrens, H. Blas, J. Vinas, C. Boissiére, C. Sanchez, M. Save, B. Charleux, Grafting polymer chains bearing an N-succinimidyl activated ester end-group onto primary amine-coated silica particles and application of a simple, one-step approach via nitroxide-mediated controlled/living free-radical polymerization, J. Polym. Sci., Part A: Polym. Chem. 48 (1) (2010) 173–185, https://doi.org/10.1002/pola.23775.
- [47] A. Rimola, D. Costa, M. Sodupe, J.-F. Lambert, P. Ugliengo, Silica Surface Features and Their Role in the Adsorption of Biomolecules: Computational Modeling and Experiments, Chem. Rev. 113 (6) (2013) 4216–4313, https://doi.org/10.1021/cr3003054.
- [48] L. Petit, L. Bouteiller, A. Brûlet, F. Lafuma, D. Hourdet, Responsive Hybrid Self-Assemblies in Aqueous Media, Langmuir 23 (1) (2007) 147–158, https://doi.org/10.1021/la061466j.

- [49] H.D. Bijsterbosch, M.A. Cohen Stuart, G.J. Fleer, Adsorption of Graft Copolymers onto Silica and Titania, Macromolecules 31(25) (1998) 8981– 8987, https://doi.org/10.1021/ma971794d.
- [50] F. Zhao, D. Yao, R. Guo, L. Deng, A. Dong, J. Zhang, Composites of Polymer Hydrogels and Nanoparticulate Systems for Biomedical and Pharmaceutical Applications, Nanomaterials 5 (4) (2015) 2054–2130, https://doi.org/ 10.3390/nano5042054.
- [51] Y. Liu, H. Meng, S. Konst, R. Sarmiento, R. Rajachar, B.P. Lee, Injectable Dopamine-Modified Poly(ethylene glycol) Nanocomposite Hydrogel with Enhanced Adhesive Property and Bioactivity, ACS Appl. Mater. Interfaces 6 (19) (2014) 16982–16992, https://doi.org/10.1021/am504566v.
- [52] R. Guo, X. Du, R. Zhang, L. Deng, A. Dong, J. Zhang, Bioadhesive film formed from a novel organic-inorganic hybrid gel for transdermal drug delivery system, Eur. J. Pharm. Biopharm. 79 (3) (2011) 574–583, https://doi.org/ 10.1016/j.ejpb.2011.06.006.
- [53] M. Takafuji, M.A. Alam, H. Goto, H. Ihara, Microspherical hydrogel particles based on silica nanoparticle-webbed polymer networks, J. Colloid Interface Sci. 455 (2015) 32–38, https://doi.org/10.1016/j.jcis.2015.05.034.
- [54] J. Wang, X. Li, Synthesis of polyacrylamide/modified silica composite hydrogels for synergistic complexation of heavy metal ions, Desalination and Water Treatment 53 (1) (2015) 230–237, https://doi.org/10.1080/ 19443994.2013.837000.
- [55] H. Ramadan, T. Coradin, S. Masse, H. El-Rassy, Synthesis and Characterization of Mesoporous Hybrid Silica-Polyacrylamide Aerogels and Xerogels, Silicon 3 (2) (2011) 63–75, https://doi.org/10.1007/s12633-010-9064-5.
- [56] E.C. Cho, J.-W. Kim, A. Fernández-Nieves, D.A. Weitz, Highly Responsive Hydrogel Scaffolds Formed by Three-Dimensional Organization of Microgel Nanoparticles, Nano Lett. 8 (1) (2008) 168–172, https://doi.org/10.1021/ p1072346e
- [57] Y. Kojima, A. Usuki, M. Kawasumi, A. Okada, Y. Fukushima, T. Kurauchi, O. Kamigaito, Mechanical properties of nylon 6-clay hybrid, J. Mater. Res. 8 (5) (1993) 1185–1189, https://doi.org/10.1557/JMR.1993.1185.
- [58] S.T. Jones, Z. Walsh-Korb, S.J. Barrow, S.L. Henderson, J. del Barrio, O.A. Scherman, The importance of excess poly(n-isopropylacrylamide) for the aggregation of poly(n-isopropylacrylamide)-coated gold nanoparticles, ACS Nano 10 (3) (2016) 3158–3165, https://doi.org/10.1021/acsnano.5b04083.
- [59] S. Kim, K. Hyun, J.Y. Moon, C. Clasen, K.H. Ahn, Depletion stabilization in nanoparticle-polymer suspensions: Multi-length-scale analysis of microstructure, Langmuir 31 (6) (2015) 1892–1900, https://doi.org/ 10.1021/la504578x.
- [60] T. Kusano, N. Kumano, W. Yoshimune, T. Munekata, T. Matsunaga, M. Harada, Interplay between interparticle potential and adsorption structure in nanoparticle dispersions with polymer addition as displayed by small-angle scattering, Langmuir 37 (24) (2021) 7503-7512, https://doi.org/10.1021/acs. langmuir.1c00968.
- [61] Z. Tang, Z. Zhang, Y. Wang, S.C. Glotzer, N.A. Kotov, Self-Assembly of CdTe Nanocrystals into Free-Floating Sheets, Science 314 (5797) (2006) 274–278, https://doi.org/10.1126/science.1128045.
- [62] F. Sciortino, E. Bianchi, J.F. Douglas, P. Tartaglia, Self-assembly of patchy particles into polymer chains: A parameter-free comparison between Wertheim theory and Monte Carlo simulation, J. Chem. Phys. 126 (19) (2007) 194903, https://doi.org/10.1063/1.2730797.
- [63] R. Yadav, P. Venkatesu, Functionalized carbon nanotubes modulate the phase transition behavior of thermoresponsive polymer via hydrophilichydrophobic balance, Polymer 178 (2019) 121573, https://doi.org/10.1016/ i.polymer.2019.121573.
- [64] R. Yadav, S. Kumar, P. Narang, P. Venkatesu, How does the addition of shape distinct gold nanoparticles influence on the conformational transition of poly (N-isopropylacrylamide)?, J Colloid Interface Sci. 582 (Pt B) (2021) 478–487, https://doi.org/10.1016/j.jcis.2020.08.074.
- [65] S.M. Moghimi, A.J. Andersen, D. Ahmadvand, P.P. Wibroe, T.L. Andresen, A.C. Hunter, Material properties in complement activation, Adv. Drug Deliv. Rev. 63 (12) (2011) 1000–1007, https://doi.org/10.1016/j.addr.2011.06.002.
- [66] M.A. Alam, M. Takafuji, H. Ihara, Thermosensitive hybrid hydrogels with silica nanoparticle-cross-linked polymer networks, J. Colloid Interface Sci. 405 (2013) 109–117, https://doi.org/10.1016/j.jcis.2013.04.054.
- [67] A. Kuijk, A. van Blaaderen, A. Imhof, Synthesis of Monodisperse, Rodlike Silica Colloids with Tunable Aspect Ratio, J. Am. Chem. Soc. 133 (8) (2011) 2346– 2349, https://doi.org/10.1021/ja109524h.
- [68] R.P. Murphy, K. Hong, N.J. Wagner, Synthetic control of the size, shape, and polydispersity of anisotropic silica colloids, J. Colloid Interface Sci. 501 (2017) 45–53, https://doi.org/10.1016/j.jcis.2017.04.026.
- [69] R.P. Murphy, K. Hong, N.J. Wagner, Thermoreversible Gels Composed of Colloidal Silica Rods with Short-Range Attractions, Langmuir 32 (33) (2016) 8424–8435, https://doi.org/10.1021/acs.langmuir.6b02107.
- [70] G.H. Bogush, M.A. Tracy, C.F. Zukoski, Preparation of monodisperse silica particles: Control of size and mass fraction, J. Non-Cryst. Solids 104 (1) (1988) 95–106, https://doi.org/10.1016/0022-3093(88)90187-1.
- [71] L.T. Zhuravlev, Concentration of hydroxyl groups on the surface of amorphous silicas, Langmuir 3 (3) (1987) 316–318, https://doi.org/10.1021/la00075a004.
- [72] T. Munk, S. Hietala, K. Kalliomäki, M. Nuopponen, H. Tenhu, F. Tian, J. Rantanen, S. Baldursdóttir, Behaviour of stereoblock poly(N-isopropyl acrylamide) in acetone-water mixtures, Polym. Bull. 67 (4) (2011) 677–692, https://doi.org/10.1007/s00289-011-0458-3.
- [73] A. García-Peñas, Y. Wang, A. Muñoz-Bonilla, M. Fernández-García, F.J. Stadler, Lower critical solution temperature sensitivity to structural changes in poly

- (N-isopropyl acrylamide) homopolymers, J. Polym. Sci., Part B: Polym. Phys. 57 (20) (2019) 1386–1393, https://doi.org/10.1002/polb.24881.
- [74] H.G. Schild, D.A. Tirrell, Microcalorimetric detection of lower critical solution temperatures in aqueous polymer solutions, J. Phys. Chem. 94 (10) (1990) 4352–4356, https://doi.org/10.1021/j100373a088.
- [75] K. Otake, H. Inomata, M. Konno, S. Saito, Thermal analysis of the volume phase transition with N-isopropylacrylamide gels, Macromolecules 23 (1) (1990) 283–289, https://doi.org/10.1021/ma00203a049.
- [76] E.P.K. Currie, W. Norde, M.A. Cohen Stuart, Tethered polymer chains: surface chemistry and their impact on colloidal and surface properties, Adv. Colloid and Interface Sci. 100-102 (2003) 205-265, https://doi.org/10.1016/S0001-8686(02)00061-1.
- [77] R.C. Ball, J.F. Marko, S.T. Milner, T.A. Witten, Polymers grafted to a convex surface, Macromolecules 24 (3) (1991) 693–703, https://doi.org/ 10.1021/ma00003a011.
- [78] C.M. Wijmans, E.B. Zhulina, Polymer brushes at curved surfaces, Macromolecules 26 (26) (1993) 7214–7224, https://doi.org/ 10.1021/ma00078a016.
- [79] H. Yotsumoto, R.-H. Yoon, Application of extended dlvo theory: li. stability of silica suspensions, J. Colloid Interface Sci. 157 (2) (1993) 434–441.
- [80] C.O. Metin, L.W. Lake, C.R. Miranda, Q.P. Nguyen, Stability of aqueous silica nanoparticle dispersions, J. Nanoparticle Res. 13 (2) (2011) 839–850.
- [81] A. Amiri, G. Øye, J. Sjöblom, Influence of ph, high salinity and particle concentration on stability and rheological properties of aqueous suspensions of fumed silica, Colloids Surf. A: Physicochem. Eng. Asp. 349 (1–3) (2009) 43– 54.
- [82] G. Vigil, Z. Xu, S. Steinberg, J. Israelachvili, Interactions of silica surfaces, J. Colloid Interface Sci. 165 (2) (1994) 367–385.
- [83] D. Grasso, K. Subramaniam, M. Butkus, K. Strevett, J. Bergendahl, A review of non-DLVO interactions in environmental colloidal systems, Re/Views in Environmental Science and Bio/Technology 1 (1) (2002) 17–38, https://doi. org/10.1023/A:1015146710500.
- [84] C.O. Metin, L.W. Lake, C.R. Miranda, Q.P. Nguyen, Stability of aqueous silica nanoparticle dispersions, J. Nanopart. res. 13 (2) (2011) 839–850, https://doi. org/10.1007/s11051-010-0085-1.
- [85] U. Hofmann, K. Endell, D. Wilm, Röntgenographische und kolloidchemische untersuchungen über ton, Angew. Chem.-Ger. Edit. 47 (30) (1934) 539–547, https://doi.org/10.1002/ange.19340473002.
- [86] M.R. Yalamanchili, A.A. Atia, J.D. Miller, Analysis of interfacial water at a hydrophilic silicon surface by in-situ FTIR/internal reflection spectroscopy, Langmuir 12 (17) (1996) 4176–4184, https://doi.org/10.1021/la950340b.
- [87] D.B. Asay, S.H. Kim, Evolution of the adsorbed water layer structure on silicon oxide at room temperature, J. Phys. Chem. 109 (35) (2005) 16760–16763, https://doi.org/10.1021/jp053042o.
- [88] H.E. Bergna, W.O. Roberts, Colloidal Silica: Fundamentals and Applications, 1st ed., CRC Press, 2005. https://doi.org/10.1201/9781420028706.
- [89] Z. Ahmed, E.A. Gooding, K.V. Pimenov, L. Wang, S.A. Asher, UV Resonance Raman Determination of Molecular Mechanism of Poly(Nisopropylacrylamide) Volume Phase Transition, J. Phys. Chem. B 113 (13) (2009) 4248–4256, https://doi.org/10.1021/jp810685g.
- [90] Y. Ono, T. Shikata, Hydration and Dynamic Behavior of Poly(N-isopropylacrylamide)s in Aqueous Solution: A Sharp Phase Transition at the Lower Critical Solution Temperature, J. Am. Chem. Soc. 128 (31) (2006) 10030–10031, https://doi.org/10.1021/ja063990i.
 [91] L. Tavagnacco, E. Zaccarelli, E. Chiessi, On the molecular origin of the
- 91] L. Tavagnacco, E. Zaccarelli, E. Chiessi, On the molecular origin of the cooperative coil-to-globule transition of poly (n-isopropylacrylamide) in water, Phys. Chem. Chem. Phys. 20 (15) (2018) 9997–10010, https://doi.org/ 10.1016/j.jcis.2021.07.006.
- [92] D.A. Dixon, K.D. Dobbs, J.J. Valentini, Amide-Water and Amide-Amide Hydrogen Bond Strengths, J. Phys. Chem. 98 (51) (1994) 13435–13439, https://doi.org/10.1021/j100102a001.
- [93] M.M. Deshmukh, S.R. Gadre, Estimation of n-h o-c intramolecular hydrogen bond energy in polypeptides, J. Phys. Chem. 113 (27) (2009) 7927–7932, https://doi.org/10.1021/jp9031207.
- [94] D.M. Carey, G.M. Korenowski, Measurement of the Raman spectrum of liquid water, J. Chem. Phys. 108 (7) (1998) 2669–2675, https://doi.org/10.1063/ 1.475659.
- [95] S.A. Deshmukh, S.K. Sankaranarayanan, K. Suthar, D.C. Mancini, Role of solvation dynamics and local ordering of water in inducing conformational transitions in poly (n-isopropylacrylamide) oligomers through the lcst, J. Phys. Chem. B 116 (9) (2012) 2651–2663, https://doi.org/10.1021/jp9031207.
- [96] H. Ohta, I. Ando, S. Fujishige, K. Kubota, A 13C PST/MAS NMR study of poly (N-isopropylacrylamide) in solution and in the gel phase, J. Mol. Struct. 245 (3) (1991) 391–397, https://doi.org/10.1016/0022-2860(91)87113-V.
- [97] A. Beganskiene, V. Sirutkaitis, M. Kurtinaitiene, R. Juškenas, A. Kareiva, FTIR, TEM and NMR investigations of stöber silica nanoparticles, Mater. Sci. 10 (4) (2004) 287-290, https://doi.org/10.5755/j01.ms.10.4.26643
- [98] C. Sronsri, K. U-yen, W. Sittipol, Analyses of vibrational spectroscopy, thermal property and salt solubility of magnetized water, J. Mol. Liq. 323 (2021) 114613, https://doi.org/10.1016/j.molliq.2020.114613.
- [99] S.M. Alahmadi, S. Mohamad, M.J. Maah, Synthesis and Characterization of Mesoporous Silica Functionalized with Calixarene Derivatives, Int. J. Mol. Sci. 13 (10) (2012) 13726–13736, https://doi.org/10.3390/ijms131013726.
- [100] M. Koyama, T. Hirano, K. Ohno, Y. Katsumoto, Molecular Understanding of the UCST-Type Phase Separation Behavior of a Stereocontrolled Poly(N-

- isopropylacrylamide) in Bis(2-methoxyethyl) Ether, J. Phys. Chem. B 112 (35)
- (2008) 10854–10860, https://doi.org/10.1021/jp800759w.
 [101] M.H. Futscher, M. Philipp, P. Müller-Buschbaum, A. Schulte, The role of backbone hydration of poly(n-isopropyl acrylamide) across the volume phase transition compared to its monomer, Sci. Rep. 7 (1) (2017) 17012, https://doi. org/10.1038/s41598-017-17272-7
- [102] P. Kujawa, F. Segui, S. Shaban, C. Diab, Y. Okada, F. Tanaka, F.M. Winnik, Impact of End-Group Association and Main-Chain Hydration on the Thermosensitive Properties of Hydrophobically Modified Telechelic Poly(Nisopropylacrylamides) in Water, Macromolecules 39 (1) (2006) 341-348, https://doi.org/10.1021/ma051876z.
- [103] J.R.S. Brownson, M.I. Tejedor-Tejedor, M.A. Anderson, FTIR spectroscopy of alcohol and formate interactions with mesoporous TiO2 surfaces, J. Phys. Chem. B 110 (25) (2006) 12494-12499, https://doi.org/10.1021/jp0614547.
- [104] M.S.C. Barreto, E.J. Elzinga, L.R.F. Alleoni, The molecular insights into protein adsorption on hematite surface disclosed by in-situ ATR-FTIR/2d-COS study, Sci. Rep. 10 (1) (2020) 13441, https://doi.org/10.1038/s41598-020-70201-z.
- [105] K. Kubota, S. Fujishige, I. Ando, Solution Properties of Poly(Nisopropylacrylamide) in Water, Polym. J. 22 (1) (1990) 15-20, https://doi. rg/10.1295/polymj.22.15.
- [106] F.E. Antunes, L. Gentile, L. Tavano, C.O. Rossi, Rheological Characterization of the Thermal Gelation of Poly(n-isopropylacrylamide) and Poly(nisopropylacrylamide) Co-acrylic Acid, Applied Rheology 19 (2009) 42064-1 42064-9. doi:10.1515/arh-2009-0014.
- [107] D. Portehault, L. Petit, N. Pantoustier, G. Ducouret, F. Lafuma, D. Hourdet, Hybrid thickeners in aqueous media, Colloids Surf. A Physicochem. Eng. Asp. 278 (1-3) (2006) 26-32, https://doi.org/10.1016/j.colsurfa.2005.11.089.
- [108] C. Karakasyan, S. Lack, F. Brunel, P. Maingault, D. Hourdet, Synthesis and rheological properties of responsive thickeners based on polysaccharide architectures, Biomacromolecules 9 (9) (2008) 2419-2429, https://doi.org/ 10.1021/bm800393s.
- [109] H. Guo, A. Brûlet, P.R. Rajamohanan, A. Marcellan, N. Sanson, D. Hourdet, Influence of topology of lcst-based graft copolymers on responsive assembling in aqueous media, Polymer 60 (2015) 164–175, https://doi.org/ 10.1016/j.polymer.2015.01.038.
- [110] M.A. Haq, Y. Su, D. Wang, Mechanical properties of PNIPAM based hydrogels: A review, Mater. Sci. and Engineering: C 70 (2017) 842-855, https://doi.org/ 10.1016/j.msec.2016.09.081.

- [111] A. Kumar, A. Srivastava, I.Y. Galaev, B. Mattiasson, Smart polymers: Physical forms and bioengineering applications, Prog. Polym. Sci. 32 (10) (2007) 1205-1237, https://doi.org/10.1016/j.progpolymsci.2007.05.003.
- [112] M. Heskins, J.E. Guillet, Solution Properties of Poly(N-isopropylacrylamide), Journal of Macromolecular Science: Part A -, Chemistry 2 (8) (1968) 1441-1455, https://doi.org/10.1080/10601326808051910.
- [113] L. Yan, Q. Zhu, P.U. Kenkare, Lower critical solution temperature of linear PNIPA obtained from a Yukawa potential of polymer chains, J. Appl. Polym. Sci. 78 (11) (2000) 1971–1976, https://doi.org/10.1002/1097-4628 (20001209)78:11<1971::AID-APP170>3.0.CO;2-P.
- [114] K.C. Etika, L. Liu, M.A. Cox, J.C. Grunlan, Clay-mediated carbon nanotube dispersion in poly(N-Isopropylacrylamide), Colloids Surf., A 489 (2016) 19-26, https://doi.org/10.1016/j.colsurfa.2015.09.024.
- [115] J. Wang, L. Lin, Q. Cheng, L. Jiang, A Strong Bio-Inspired Layered PNIPAM-Clay Nanocomposite Hydrogel, Angew. Chem. Int. Ed. 51 (19) (2012) 4676-4680, https://doi.org/10.1002/anie.201200267
- [116] T. Gan, Y. Guan, Y. Zhang, Thermogelable PNIPAM microgel dispersion as 3D cell scaffold: effect of syneresis, J. Mater. Chem. 20 (28) (2010) 5937-5944, https://doi.org/10.1039/C0JM00338G.
- [117] W. Liao, Y. Zhang, Y. Guan, X.X. Zhu, Gelation Kinetics of Thermosensitive PNIPAM Microgel Dispersions, Macromol. Chem. Phys. 212 (18) (2011) 2052-2060, https://doi.org/10.1002/macp.201100137.
- [118] J. Shen, T. Ye, A. Chang, W. Wu, S. Zhou, A colloidal supra-structure of responsive microgels as a potential cell scaffold, Soft Matter 8 (48) (2012) 12034-12042, https://doi.org/10.1039/C2SM26885J.
- [119] M. Rubinstein, R.H. Colby, Polymer physics, Vol. 23, Oxford University Press, New York, 2003.
- [120] Q. Cai, Z.-S. Luo, W.-Q. Pang, Y.-W. Fan, X.-H. Chen, F.-Z. Cui, Dilute solution routes to various controllable morphologies of MCM-41 silica with a basic medium, Chem. Mater. 13 (2)(2001) 258-263. https://doi.org/10.1021/
- [121] E.M. Björk, F. Söderlind, M. Odén, Tuning the shape of mesoporous silica particles by alterations in parameter space: From rods to platelets, Langmuir 29 (44) (2013) 13551-13561, https://doi.org/10.1021/la403201v.
- [122] R. Narayan, U.Y. Nayak, A.M. Raichur, S. Garg, Mesoporous silica nanoparticles: A comprehensive review on synthesis and recent advances, Pharmaceutics (2018)118, https://doi.org/10.3390/ (3) pharmaceutics10030118.